

TOPSIS vs MIO: Applications to gold prospectivity mapping; a case study of the Basiran-Mokhtaran area- eastern Iran

Hosein Ferdowsi ^a, Abbas Bahroudi ^{a,*}, Ali Moradzadeh ^a and Maysam Abedi ^a

^a School of Mining Engineering, College of Engineering, University of Tehran, Tehran.

Article History:

Received: 05 November 2023.

Revised: 29 November 2023.

Accepted: 31 December 2023.

ABSTRACT

As the depth of mineral exploration has increased in recent years, multiple exploration methods have become necessary to obtain more accurate depth and surface data. Each type of exploratory data has different uncertainty, resolution, and efficiency levels. Using these data individually or preparing traditional models based on a single data type often fails to meet the desired accuracy level. Therefore, mineral prospectivity mapping (MPM) has become more common in integrating these data. MPM methods require determining the importance of the data used. This importance is expressed as the weight of the layers (evidence). Typically, data-driven methods cannot be used to determine the weight of evidence layers in green areas due to the need for sufficient deposits. In these areas, knowledge-based methods, using the opinions of expert geologists, are often used to determine the weight of the layers. However, the weights determined by different experts may vary depending on their perspectives. Therefore, one of the challenges of using MPM methods in green areas is determining a reliable weight for the layers. This paper uses different exploration data, such as airborne geophysical data, geochemistry, geology, and remote sensing data, to prepare suitable reference layers. Due to the limited mineral prospects available in this area, we used the prediction-area (P-A) method to calculate the layers' weights without experts' opinions. We then used these weights to produce the gold prospectivity map in this area using the multi-index overlay (MIO) and the (Adjusted, Conventional, and Modified) TOPSIS methods. Finally, the obtained results were used to evaluate the efficiency of these methods and the calculated weights for this area.

Keywords: Mineral Prospectivity Mapping (MPM), Prediction-Area (P-A), Continues weighting, Multi-Index Overlay, TOPSIS.

1. Introduction

Mineral resources are essential drivers of progress and development in contemporary human societies. The growing demand for these resources has intensified the need to explore new mineral deposits. [1]. Since most shallow deposits or those with surface outcrops have already been discovered, exploring hidden mineralization systems has become the primary exploration strategy [2], [3]. However, detecting hidden mineralization demands comprehensive subsurface data to understand geological processes and their mass distribution at depth [4]. The advent of advanced sensors has diversified the pool of exploratory data. Diverse sensor types have provided multifaceted information sources, enriching decision-making across various disciplines [5].

Exploring concealed mineral deposits in regions with surface cover poses challenges due to limited and indirect access to relevant geological data. Typically, this dataset is based on geological, remote sensing, geophysical, and geochemical investigations. Unfortunately, incomplete and scanty information coverage makes identifying intricate relationships resulting from numerous geological processes in these regions difficult, if not impossible [6], [7]. Mineral exploration methods are tailored according to the deposit type and its characteristics. Understanding mineralization processes and identifying factors that govern the formation and preservation of a mineral deposit are pivotal in mineral exploration [8]. However, the interpretation of mineral exploration data often yields inherently uncertain results influenced by individual subjectivity. Therefore, ensuring the mineral exploration process's objectivity, quantification, and refinement is of paramount

importance in exploration science [1], [9].

Mineral exploration is a multifaceted decision-making task aimed to minimize the cost, time, and energy invested in exploration operations [10]. The quality of exploration data and the robustness of the conceptual model have significant influence over the effectiveness of these decisions [11]. Given the potential for enhanced accuracy and resolution through multi-sensor data utilization, coupled with the complexity of parameters influencing mineral deposit formation, the integration of information layers is highly crucial in generating prospective mineral maps [12], [13]. These MPMs typically result from a fusion of evidence (or predictor) maps [14] that comprise a set of exploratory criteria (mappable proxies) defined by measurable spatial associations related to the target deposit [8], [15]. Geoscientific datasets are formed and selected based on the conceptual mineralization model specific to the deposit type [16]. Subsequently, these chosen layers undergo weighting and combination processes [17], [18].

The method for assigning weights to index features depends on the presence or absence of known mineral occurrences in the study area. Data-driven approaches are appropriate for brownfields with an adequate number of known mineral occurrences used to determine the weight of reference layers [11], [18], [19]. In green areas, where mineral occurrences are scarce, criteria layers are weighed using a knowledge-driven method, relying on the expert's subjective judgment [20], [21]. Additionally, hybrid methods have emerged, combining data-driven and knowledge-driven methods to address these challenges [22]. Another

* Corresponding author. E-mail address: A.Bahroudi@ut.ac.ir (A. Bahroudi).

class of MPM methods utilizes logistic functions suited for the purpose [23]. These methods employ sigmoid logistic functions and continuous data to generate witness maps essential for assessing mineral deposit potential [11], [24].

In this paper, we applied the MPM methodology to assess the gold potential within the porphyry-hydrothermal system of the Mokhtaran-Basiran area, situated in the Lut block and the Flysch zone of eastern Iran. Renowned for its complex geological setting and mineralization history, this area poses a formidable challenge for gold exploration. We aim to identify and map key factors influencing gold deposit formation in porphyry-hydrothermal systems, including magmatism, tectonics, alteration, and geochemistry. These factors serve as spatial proxies, generating input layers for MPM analysis. We employed two GIS-based models, multi-index overlay and TOPSIS, to integrate these input layers with assigned weights, ultimately producing MPM maps illustrating the spatial distribution of gold potential zones within the study area.

2. 2. Geological Setting

The study area is in eastern Iran, encompassing portions of the 1:100,000 geologic maps of Mokhtaran, Basiran, and Koudkan. The location of the study area is depicted in Figure 1, which illustrates the geologic map of Iran (revised after Alavi and Aghanabati [25], [26]). The region is tectonically complex, owing to its position within two significant structural units of Iran: The Sistan suture zone and the Lut block. Eastern Iran occupies a complex and active geological domain where three tectonic plates converge: Arabian, Eurasian, and Indo-Australian. Throughout history, this region has joined the Lut and Afghan blocks and experienced numerous geological events. The collision between these plates, influenced by the Alpine orogeny, has resulted in folds, faults, and significant thrusting [27]–[29].

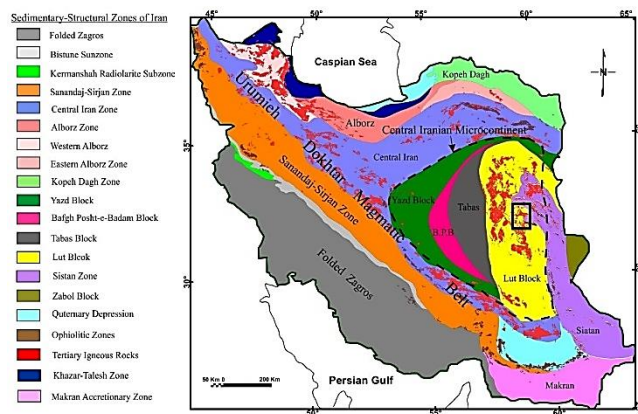


Fig. 1. The location of the study area on the simplified structural geological map of Iran (modified after Alavi, 1991 and Aghanabati, 2005) [25], [26].

The Sistan rift zone is a strongly folded and faulted mélangé flysch basin. The border of this zone is in the east of the Hariroud fault, which almost coincides with the border of Iran and Afghanistan, and in the west, it is separated from the Lut block by the Nahbandan fault [28], [30], [31]. The Sistan zone is highly tectonized, and it is believed to be the accretionary prism of the Neotethys Ocean, which was created and closed during the Late Cretaceous–Paleozoic. The ophiolitic-felsic mixture complex of eastern Iran formed as this oceanic crust subducted under the Lut block [31]–[33]. This zone includes two sets of ophiolitic mélangé (the Retok set in the west and Neh in the east), which are separated by a sedimentary basin (the Sefidabeh basin) [28], [34]. The overall lithology in this zone includes felsic rocks, volcanic rocks, sedimentary-volcanic rocks, ophiolites, and intrusive rocks. The Sistan zone includes thick deep-sea sediments such as argillitic and siliceous shales, radiolarite and pelagic limestone, and volcanic rocks such as basalt, diabase, andesite, dacite, rhyolite, and ultramafic secondary rocks.

The bedrock is probably composed of oceanic crust [26], [35].

The Lut block is a microcontinent separated from northern Gondwana during the Permian to Triassic periods due to tectonic movements and developed in an extensional environment [36], [37]. Geographical features, such as the Drouneh fault to the north and the Jazmorian depression to the south, bound this block. On its eastern side, the Nehbandan fault acts as a separator from the Flysch zone, while its western edge is marked by the Nayband fault and the Shotori mountains, which distinguish it from central Iran [26]. The Lut Block involves a pre-Jurassic metamorphic basement, Jurassic sedimentary rocks, and several generations of late Mesozoic and Cenozoic intrusive and volcanic rocks [27], [28]. Most of the Lut block comprises Tertiary alkaline and calc-alkaline volcanic-magmatic rocks of varying ages, spanning from the Eocene to the Oligocene [38]. The earliest magmatic activity within the Lut block traces back to the Jurassic period, reaching its peak during the Tertiary period [38]. This geological history is characterized by various granite formations, including notable ones like the Red Mountain, as well as Mount Shakhkouh and Mount Bidmeshk. The Tertiary magmatic activity in this region encompasses volcanic and plutonic phases, with volcanic activity commencing during the Late Cretaceous and reaching its peak in the Eocene [39].

Eocene volcanic and pyroclastic lavas outcrop in the central part of the area include andesite-basalt volcanic flows as well as black tuff and dacitic tuffs with coarsely porphyritic trachytic andesite flows. The Eocene volcanic units are cut by granitoids, dykes, and small dacitic bodies. Valuable minerals such as lead, copper, iron, and gold are formed at the contact surface of these bodies, especially dacitic units with pyroclastic and volcanic Eocene rocks [40], [41].

Due to the many magmatic activities and special geological conditions that have existed in the Lut block at different times, various mineralization systems such as porphyry, epithermal, and vein type deposits have occurred in this block [42]. The Maherabad and Khopik porphyry gold copper deposits, the Shorab and Khonik epithermal gold deposits, and the Qala Zari iron-oxide-copper-gold (IOCG) deposit are the important and prominent deposits in this area [42], [43]. These deposits and their tectonic history make this area significant for undiscovered deposits.

Figure 2 shows a simplified geologic map of the study area. Most of the rocks in the northern part of the area, which is the junction of the Lut block and the Flysch zone, have experienced metamorphism of different intensities due to tectonic and thrust processes. Flysch rocks and colored mélangé belts with the Upper Cretaceous age are the most abundant in this area. Ultrabasic rocks (peridotite and serpentinite), diabase, and diabasic tuffs are rich in these structures. Some red-brown listwanite outcrops are exposed with a distinct border from mélanges. The sedimentary layers within the mélanges have felsic sequences. In the northern part, the metamorphosed remnants of the pre-Cretaceous Shakhkouh granite can be seen in the form of extensive lenses of granite, gneiss, and schist. By moving to the south, the mélanges of these hills gradually become older and closer to the Lut block [41].

A significant part of the area is also covered by Quaternary sediments, which are usually in the form of hills with low topography. These deposits are mostly composed of sandstone, gray, black, and green shale, which in some places are covered with silt, marble, marl, conglomerate, and coal shale layers. Gray quartzite sandstone is also found in these formations. Black andesitic lavas cover the shale and sandstone units, the thickness of which reaches 250 m in some places [40]. Alluviums are mainly composed of gravel cones, salt and mud domes, sand dunes, river terraces, clay deposits, salt beds, and channel bed deposits [41].

3. Materials and methods

This study started by gathering the existing data related to the area, such as airborne geophysical, geochemical, geological, and remote sensing data. Then, the relevant layers were selected based on the conceptual model and the exploration information system, and these layers were extracted from the data as evidence layers. These layers were then collected in a GIS database using the WGS 84 datum UTM zone

40 coordinate system. Next, the fractal method was applied to identify the influences between these evidence layers (proxies) and the known mineralization events in the study area. A weight was assigned to each proxy using the prediction-area method. After that, the evidence layers were combined and integrated according to their weights using the TOPSIS and multi-index overlay methods. Finally, the gold prospects were identified and then the results were evaluated. Below, the main steps of our work are explained.

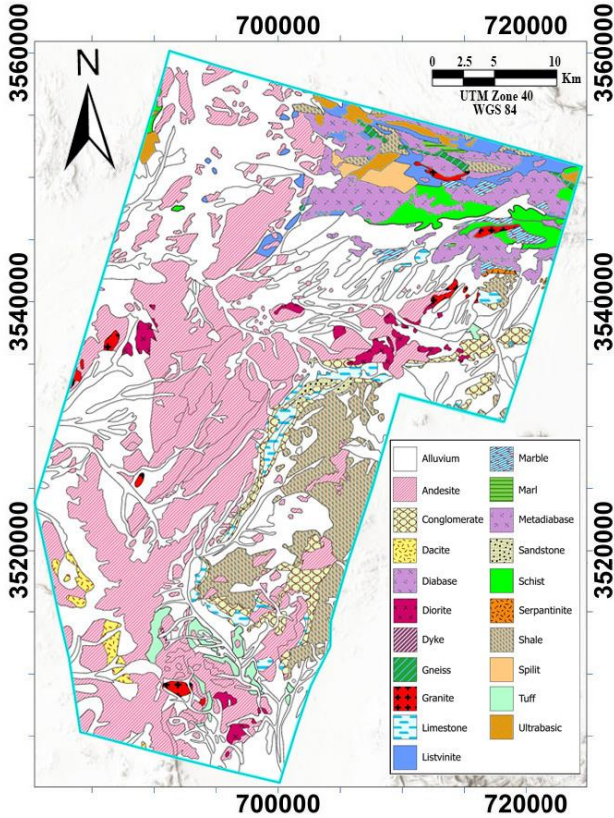


Fig. 2. Simplified Geological map of the study area.

3.1. Creating continuous layers

Multi-criteria decision-making methods (MCDM) integrate various criteria for evaluation, necessitating the need to scale these criteria before integration. Consequently, normalizing the input data within a specific interval becomes necessary in the context of MCDM methods. In this research, to enhance accuracy and eliminate errors in classifying the values within each layer, we utilized continuous data within the interval [0,1] known as fuzzy evidence layers [44]–[46]. To achieve this, we employed the logistic function (Eq. 1) to standardize the evidence layers to the same interval [0,1].

$$f_{ij} = \frac{1}{1 + e^{-s(x_{ij} - b)}} \quad (1)$$

In equation (1), x_{ij} is the value of each cell before, and f_{ij} is its value after transformation; b and s are the inflection point and the slope of the logistic function, respectively [45], [47], [48].

3.2. Weight determination method

When conducting a mineral prospectivity modeling, the assigned weight for a spatial evidential layer should take into account its relationship with the type of mineralization being sought [48]. Assessing the effectiveness of prospecting methods often involves analyzing the location of mineral occurrences in the study area.

Therefore, it is important to establish the number of known deposits in the selected evidential class. Fractal analysis has proven useful in studying the connection between specific mineralization and geological, structural, and geochemical factors related to different spatial reference layers [47], [49]. This study utilized the multi-fractal Concentration-Area (C-A) method (Eq. 2) to identify threshold limits for classifying the layers and assigning the weights to each layer.

$$\begin{cases} A(\rho \leq v) \propto \rho^{-\alpha_1} \\ A(\rho > v) \propto \rho^{-\alpha_2} \end{cases} \quad (2)$$

Where $A(\rho)$ corresponds to the surface area of regions that are at or below the breaking point (threshold) v , while α_1 and α_2 indicate the lowest and highest powers, respectively [47].

An effective MPM should possess the capability to anticipate the maximum number of mineral prospects within the smallest geographical extent [18]. This is the foundational principle for demonstrating the relative importance and predictability of evidential layers concerning a specific deposit. Consequently, the allocation of weights to various layers can be established using P-A diagrams, as indicated in previous research studies [24], [50].

In this study, the weight assigned to each layer was determined by identifying the intersection point on the P-A diagram. This diagram comprises two curves: one representing the percentage of predicted known deposits based on the categories derived from the C-A diagram and the other depicting the proportion of areas associated with each category. The weight attributed to a layer is established by pinpointing the intersection between these curves [24], [51].

To quantitatively determine the weight assigned to each evidential layer, we calculated the logarithm of the predicted rate divided by the corresponding area coverage at the intersection point on the P-A diagram, as specified in equation (3) [50], [52].

$$W_E = \ln\left(\frac{P_r}{O_a}\right) \quad (3)$$

Where W_E is the weight assigned to each proxy, P_r is the prediction rate, and O_a is the engaged area of the P-A chart. This study removed the layers with negative weights from the integration process.

3.3. Integration of evidential maps

The evidence layers were first prepared and then transformed into continuous fuzzy evidence layers by applying the sigmoid logistic function to each layer's values. Once the weight of each layer was determined, they were merged to create a prospective map using either the MIO or the TOPSIS method, as described below.

3.3.1. Multi-Index Overlay (MIO) method

The MIO method is a commonly used knowledge-based method for integrating evidence layers and producing MPMs. This method was developed to integrate layers that have several separate classes. In this method, evidential layers with several discrete classes can be purposefully integrated by considering the weight of the layer. In this study, each cell in each layer was considered as a class, and the existing layers were merged using equation (4):

$$MIO = \frac{\sum_i^n T_{vi} w_i}{\sum_i^n w_i} \quad (4)$$

T_{vi} , W_i , and MIO, respectively, represent the cell value, the weight of layer i , and the cell value of the final integrated layer [18], [45], [50], [53].

3.3.2. TOPSIS Method

The TOPSIS (Technique for Order Preference by Similarity to Ideal Solution) method is one of the most effective, well-known, and popular MCDM methods that was first used by Hwang in 1981. It was further developed by Yoon in 1987 and Hwang in 1993. The TOPSIS method involves defining a Positive Ideal Solution (PIS) and a Negative Ideal Solution (NIS). The PIS is the maximum in positive features (benefits)

and the minimum in negative features (costs), while the NIS represents the opposite. The available alternatives are then ranked based on their proximity to the PIS and distance from the NIS. The TOPSIS method includes three different common approaches (conventional, adjusted, and modified TOPSIS) that differ slightly. The steps to implement this method are summarized below [54]–[57].

3.3.2.1. Common TOPSIS (C-TOPSIS) method

To implement this method, the following steps are performed.

1- Creating $X=(x_{ij})_{m \times n}$ as a decision matrix consisting of m alternatives and n criteria

2- Calculating the normalized decision matrix $R=(r_{ij})_{m \times n}$ using Eq. (5)

$$r_{ij} = \frac{x_{ij}}{\sqrt{\sum_{k=1}^n x_{kj}^2}} \quad \text{for } i = 1, 2, \dots, m \text{ and } j = 1, 2, \dots, n \quad (5)$$

Where w_j is the weight of each evidence layer so that $\sum_{j=1}^n w_j = 1$.

4- Determine the PIS and NIS as eq. (7 and 8)

$$\begin{aligned} \text{PIS} &= \{t_j^+ | j=1, 2, \dots, n\} = \{[\max(t_{ij} | i=1, 2, \dots, m) | j \in B], \\ &[\min(t_{ij} | i=1, 2, \dots, m) | j \in C]\} \end{aligned} \quad (7)$$

$$\begin{aligned} \text{NIS} &= \{t_j^- | j=1, 2, \dots, n\} = \{[\min(t_{ij} | i=1, 2, \dots, m) | j \in B], \\ &[\max(t_{ij} | i=1, 2, \dots, m) | j \in C]\} \end{aligned} \quad (8)$$

Where B and C represent the benefit and cost criteria, respectively.

Calculating the Euclidean distance of any alternative with the PIS as S_i^+ and the NIS as S_i^- respectively using Eq. 9 and 10:

$$S_i^+ = \sqrt{\sum_{j=1}^n (t_{ij} - t_j^+)^2} \quad (9)$$

$$S_i^- = \sqrt{\sum_{j=1}^n (t_{ij} - t_j^-)^2} \quad (10)$$

6- Calculating the relative proximity of alternatives to the ideal solution by Eq. (11)

$$T_i^c = \frac{S_i^-}{S_i^+ + S_i^-} \quad (11)$$

7- Computing the normalized score

$$M_i^c = \frac{T_i^c - \min(T_i^c)}{\max(T_i^c) - \min(T_i^c)} \quad i = 1, 2, \dots, m \quad (12)$$

3.3.2.2. Adjusted TOPSIS (A-TOPSIS) method

The adjusted TOPSIS (A-TOPSIS) method was introduced in 2000 by Deng et al. The procedure of implementing this method is similar to that of C-TOPSIS, only steps 4 and 5 have been changed as follows [55], [58].

4- The determination of the PIS and NIS is undertaken as detailed in Eq. (13) and Eq. (14), respectively

$$\begin{aligned} \text{PIS} &= \{r_j^+ | j=1, 2, \dots, n\} = \{[\max(r_{ij} | i=1, 2, \dots, m) | j \in B], \\ &[\min(r_{ij} | i=1, 2, \dots, m) | j \in C]\} \end{aligned} \quad (13)$$

$$\begin{aligned} \text{NIS} &= \{r_j^- | j=1, 2, \dots, n\} = \{[\min(r_{ij} | i=1, 2, \dots, m) | j \in B], \\ &[\max(r_{ij} | i=1, 2, \dots, m) | j \in C]\} \end{aligned} \quad (14)$$

Where r_{ij} is the normalized decision matrix.

5- To compute the weighted Euclidean similarity distance of any alternative, two distances are calculated: one with respect to the PIS (designated as S_i^+) using Eq. (15), and the other for the NIS (denoted as S_i^-) employing Eq. (16).

$$S_i^+ = \sqrt{\sum_{j=1}^n w_j (r_{ij} - r_j^+)^2} \quad (15)$$

$$S_i^- = \sqrt{\sum_{j=1}^n w_j (r_{ij} - r_j^-)^2} \quad (16)$$

It is essential to note that the remaining steps in this approach is closely similar to those of the C-TOPSIS method.

3.3.2.3. Modified (M-TOPSIS) method

The Modified version of the TOPSIS method (M-TOPSIS) was introduced by Wren in 2007, specifically designed to address ranking challenges when dealing with alternatives closely resembling either positive or negative alternatives. This approach closely mirrors the C-TOPSIS method in most of its steps, with the exception of the 6th step, where a modification involves the use of the Euclidean distance as the key metric. The details of these modifications are delineated as follows [59]:

Step 6: In this step, the initial Ideal Alternative (denoted as "S") is determined using Eq. (17), followed by the computation of a similarity distance metric using Eq. (18).

$$S = (S^{lp}, S^{gn}) = (\min(S^+_i), \max(S^-_i)); i = 1, 2, \dots, n \quad (17)$$

$$T_i = \sqrt{(S^+_i - S^{lp})^2 + (S^-_i - S^{gn})^2}; i = 1, 2, \dots, n \quad (18)$$

4. Used evidence layers

To explore gold in the study area, we prepared the evidence layers by processing geological, geophysical, and geochemical data, and satellite images. These layers were then placed in a geographic database in the form of a grid of 100-meter square cells. The process for preparing these layers is detailed below.

4.1. Known mineral deposits

This study focuses on active mines, proven mineral deposits, and mineralized outcrops indicated on the 1:100K and 1:250K geologic maps listed in Table 1. To avoid any bias caused by having multiple mineral types in a particular region, the point data were selected with a minimum distance of 500 m between each point [60]. As a result, the number of prospects reduced from 21 to 19 points.

Table 1. Known Gold Deposit in the Study Area.

FID	x	y	Name	Index Type
1	681785	3523046	Koudakan	Mine
2	690588	3520649	Qaleh Zari Anomaly	Mine
3	707724	3537157	Hurideh Anomaly	Index
4	692074	3525606	Chahvak	Au
5	703778	3512213	Bisheh Anomaly	Index
6	703785	3537950	Hired	Index
7	705518	3537111	Hired3	Au Epithermal
8	708106	3541570	Hired1	Au Epithermal
9	708224	3535841	Hired	Deposit
10	709828	3537045	Hired	Cu, Au
11	708388	3553501	Hangaran Anomaly	Index
12	709532	3551460	Listvenite Mokhtaran	Listvenite
13	712364	3551518	Listvenite Mokhtaran	Listvenite
14	690547	3556632	Listvenite Mokhtaran	Listvenite
15	716597	3543688	Chah Zaghu	Deposit
16	689538	3519021	Qaleh Zari	Index
17	710783	3551825	Mokhtaran	Deposit
18	687664	3520263	Qaleh Zari	Index
19	686690	3513043	Chah Shalghmi	Deposit

4.2. Geological layer

More than 50% of the geologic map of the area is covered by the Quaternary alluvial sediments, with Andesitic units covering 23% of the map. This poses a challenge for mineral prospecting in the area, underscoring the importance of subsurface data. Researchers correlate known gold deposits with lithology to determine the significance of geological units in a region. The results showed that six gold indications were found on Cretaceous units, seven on Eocene-Oligocene units, and five on Quaternary sediments. In terms of lithology, there are five deposits in alluvial units, six deposits in andesitic units, and six deposits in intrusive rocks. Intrusive rocks play a crucial role in gold mineralization in the study area, with six deposits found on these rocks despite their minimal surface areas. As a result, the inverse distance from intrusive rocks is used in the prospectivity mapping process as one of the standard layers. A score was assigned to the geological layer based on the intersection point of two graphs in the P-A chart; it was found that 58% of known Au prospects are located on only 42% of the area, giving this layer a weight of 0.32. Figure (3) shows the results of our analysis for the intrusive score evidence layer. The figure is divided into four parts: (a) a map of the intrusive score evidence layer in continuous

form, (b) the C-A chart for this map, (c) a discretization map based on C-A of map (a), and (d) the P-A chart for map (c).

4.3. The geochemical layer

Geochemical anomaly mapping involves identifying anomalous concentrations of pathfinder and indicator elements in different sampling media to locate undiscovered mineralized zones. Stream sediment geochemical studies have been the most cost-effective way to sample large terrain areas for geochemical surveys. This helps to identify areas for further investigations [61], [62].

In this study, our analysis focused on data from stream sediment geochemical studies carried out by the Geological Survey of Iran (GSI) over three 1:100K geologic maps: Basiran, Koudkan, and Mokhtaran. The GSI collected 2468 stream sediment samples, with 645 of these located in our study area. The Inductively Coupled Plasma-Optical Emission Spectrometry (ICP-EOS) method was utilized to analyze Cu, Ag, Sn, Pb, Zn, Sr, Sb, and Hg, and the Fire assay method to analyze Au. After pre-processing the data, we created element distribution maps, which helped us identify anomalous areas and precisely interpret each target.

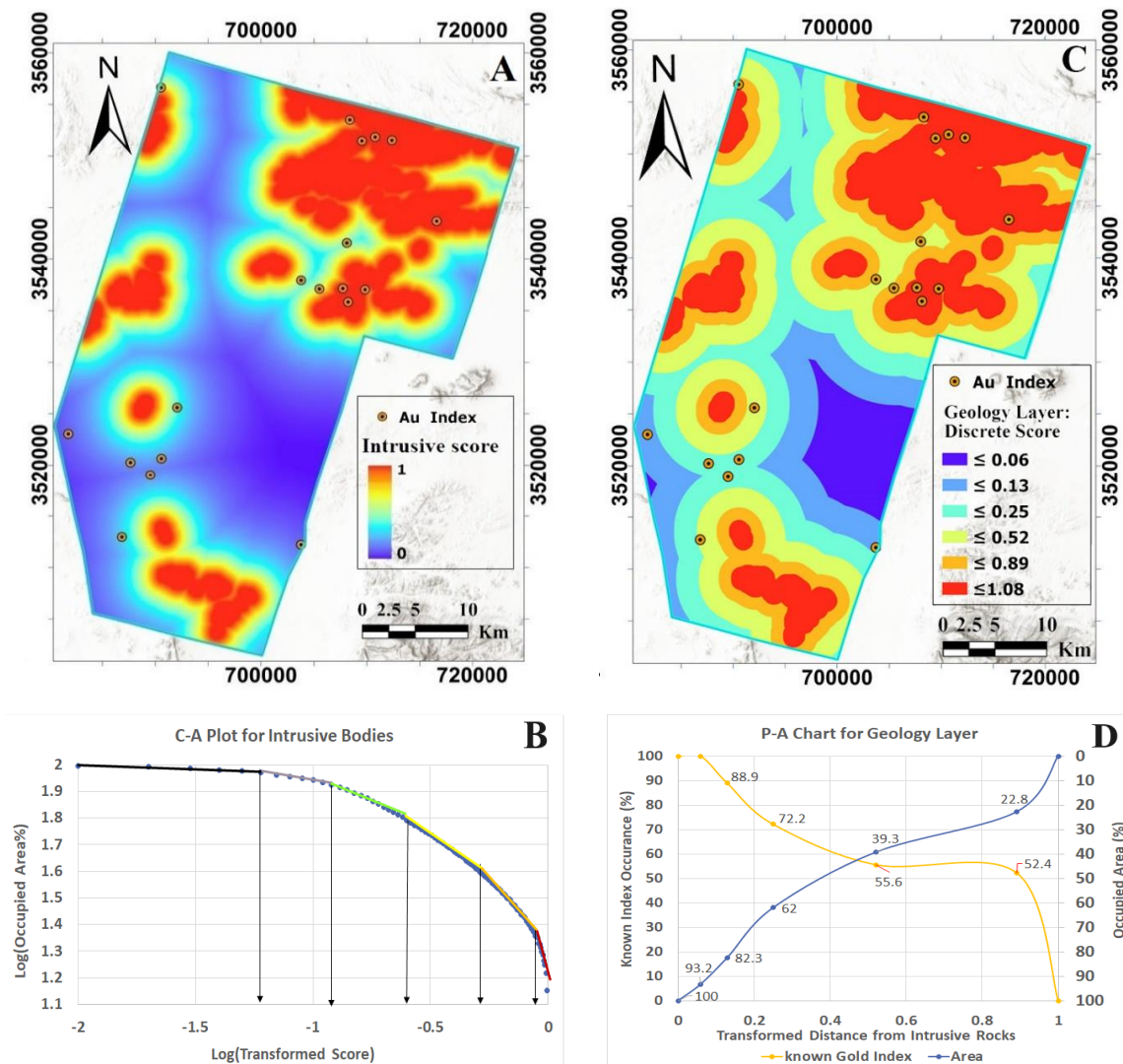


Fig. 3. Maps and charts for Intrusive score proxy layer -A) Continuous map. -B) C-A chart of map (A). -C) Discrete map of intrusive score used for weight calculation. -D) P-A chart of intrusive score.

The data of each sheet is processed separately. First, the catchment correction was used to attribute anomalies to their corresponding upstream lithological unit. The Concentration-Area diagram was then utilized to separate anomalies from background values and categorize them. Correlation testing revealed a high correlation among Ag, Cu, and Au. These processes, along with univariate and multivariate statistical methods, effectively determined the geochemical anomalies. Factors such as silver, gold, bismuth, copper, lead, and zinc were selected through factor analysis and Pearson's correlation test to prepare the geochemical layers. The weight of these layers was determined using the C-A and P-A charts, and the desired geochemical evidential layer was obtained by combining them through the MIO method [63].

To determine the weight of the geochemical evidential layer, we first used the C-A diagram (Fig. 4B) to establish the threshold values. Using the P-A diagram (Fig. 4D), we found the intersection point (71, 29), which gave the geochemical evidential layer a weight of 0.89, indicating its importance. Figures 4 (a)-(d) display the steps to prepare the evidential map of the geochemistry layer.

4.4. Remote sensing layer

The exploration of mineral deposits, including massive sulfide, epithermal, porphyry, and IOCG deposits in green areas, has been greatly aided by using satellite imagery. The mineralization system is

typically associated with altered zones within and around the deposits. One significant difference between fresh and altered zones is the presence of alteration minerals, like allunitite, montmorillonite, kaolinite, etc., inside the altered rocks. These minerals can result in slight variations in the value of received waves to the sensing device, depending on their spectral characteristics [64]–[66].

We analyzed satellite images from Landsat and ASTER to investigate changes in the study area. We selected ASTER images from two LIT scenes, 00305052003065556_20150429133528_37334 and 00305052003065605_20150429133531_109762, which can be found at <https://earthdata.nasa.gov>. These scenes provided minimal cloud cover in the study area. For Landsat, we used images from the Landsat 8 scene, LC08_L1TP_159038_20190101_20190101_01_RT, collected by Operational Land Imager (OLI) sensors. Although some clouds were present in the northern part of the area, the overall cloud cover was less than 5% for the entire study area.

The Landsat 8 and ASTER data were processed and preprocessed using the ENVI software. We used the FLAASH module to correct atmospheric errors in the Landsat 8 OLI and ASTER images. We used the PCA approach and the band ratio method for the iron oxide alteration in Landsat ETM 8 scenes. To detect Phyllic, Argillic, Potassic, Silicic, and Propylitic alterations from ASTER images, we used the PCA, band ratio, and Spectral Angle Mapper (SAM).

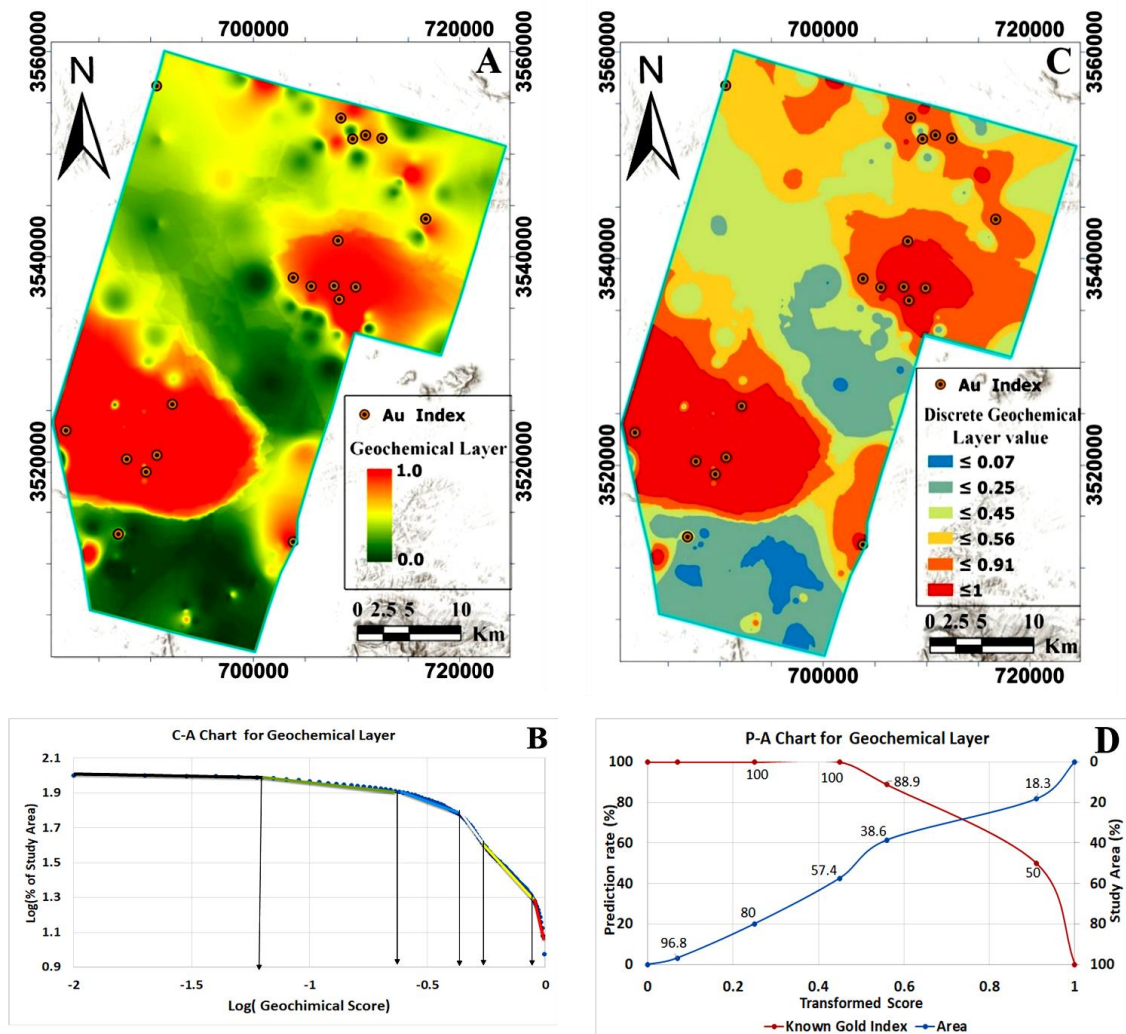


Fig. 4. Maps and charts for geochemistry proxy layer -A) Continuous map. -B) C-A chart of map (A). -C) Discrete map Used for weight calculation. -D) P-A chart of geochemistry score.

The logistic function transforms every alteration layer into a range of [0, 1]. The weight of each layer is calculated using the P-A method for known gold indications in the area. The Phyllic, Silicic, Iron oxide, and Propylitic layers have weights of 0.24, 0.58, 0.28, and 0.6, respectively. The Potassic alteration has a negative weight, and the Argillic layer has a very low weight of 0.08, indicating a weak relationship with gold mineralization in this area. The above-mentioned alteration layers are combined using the MIO method (eq. 11) to produce the integrated RS map. The weight of the RS map for gold potential mapping in the study area is calculated to be 0.62 (Figure 5). This means the remote sensing map accurately predicted 65% of the gold occurrences in 35% of the study area.

4.5. Airborne geophysics data

Airborne geophysical data has proven invaluable for extracting geological information from areas that would otherwise be difficult to access due to extreme topography or sediment coverage. This data has provided researchers with crucial insights into the distribution of subsurface masses, leading to significant breakthroughs in mineral exploration. Mineral deposits form when fluids interact with the rocks that serve as their host. During this process, the environment's physical properties change, and the rocks' primary minerals are altered. [67]–[70].

The airborne dataset used in this study was collected by the GSI in 2013. The flights were carried out on a flight line spacing of 250 meters

at azimuths 105 and 285 degrees. The ties were spaced 3 km apart at azimuths 15 and 195 degrees. The helicopter's flight and radiometric altitude was 60 m above the ground level, the magnetic sensor altitude was about 45 m, and the electromagnetic data height was about 30 m.

4.5.1. Airborne magnetic data

A magnetic Cesium Vapor sensor with a 10 Hz sampling rate was installed on the bird and was located 15 meters below the helicopter for optimal sampling. The data was meticulously prepared, undergoing various corrections such as Diurnal, Lag, and Heading, and was further processed through IGRF, leveling, and micro-leveling techniques. Then, the Reduction to the magnetic Pole grid allowed for precisely identifying magnetic lineaments and shallow bodies. Additional information on these processes will be provided below.

4.5.1.1. Magnetic Lineament Layer

Faults and fractures can act as a pathway for mineral-rich fluids below the earth's surface. These pathways play an important role in forming mineral deposits by transporting valuable minerals from the mantle and/or crust to areas where they can be deposited [52]. Faults and fractures can bring rocks with different magnetic properties into linear contact, showing an abrupt change in magnetic properties. This makes it possible to detect hidden faults by detecting magnetic lines [67], [71]–[74].

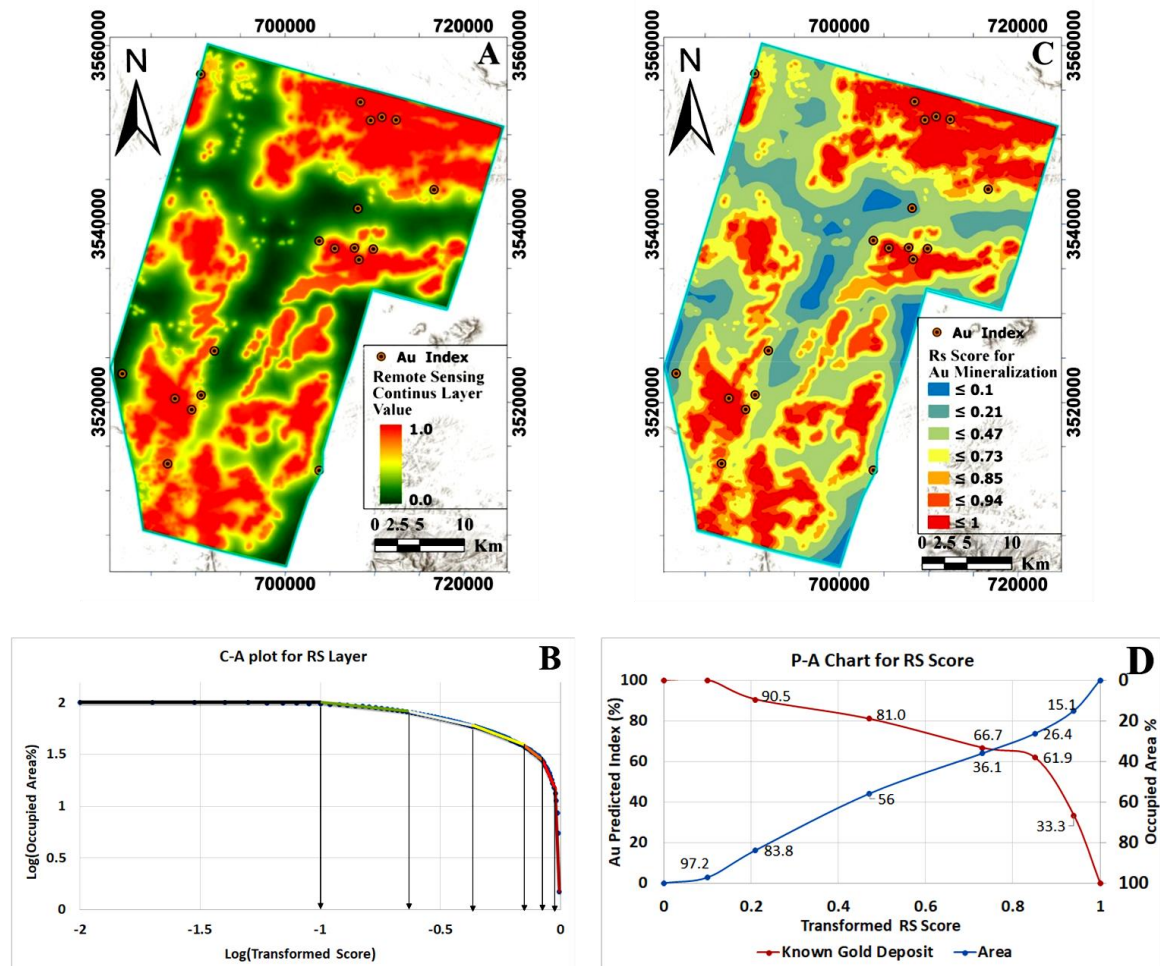


Fig. 5. Maps and charts for Remote Sensing Proxy Layer -A) Continuous map. -B) C-A Chart of Map (A). -C) Discrete Map Used for Weight Calculation. -D) P-A Chart of Remote Sensing layer.

A combination of filters, including the first-order vertical derivative, total horizontal derivative, analytical signal, and tilt angle, were utilized to identify magnetic lineaments. The automatic separation method was applied to highlight these lineaments. The faults provided in geologic maps were combined with these lineaments using an OR fuzzy operator. A density map of lineaments was then generated based on the size and number of lineaments within each cell. Normalizing the map using a sigmoid function (Eq. 1) created a density layer of lineaments. Figure 6 (a-d) depicts a lineament evidential map generated from airborne magnetic data. The intersection point of the two curves predicted a 65% gold prospect rate with an equivalent area of 35% and a weight of 0.62.

4.5.1.2. Magnetic shallow bodies

Intrusive sources can produce fluids and dissolved constituents like salts, gases, and metals. These sources are often highly fractured near the contact, which allows hydrothermal fluids to pass through and exchange heat and mass with the intrusive rocks [75]–[78]. Identifying the structures such as contacts, lineaments, and shallow bodies is essential for locating a mineralization system. The aeromagnetic approach is

useful for this purpose, and various filters have been used to investigate buried source boundaries. Techniques like First Vertical Derivative, Total Horizontal Derivative, Analytic Signal, and Tilt Angle can be employed to achieve the goals of these studies [79], [80].

We drew the magnetic shallow bodies with the use of the filters mentioned above. Then, we calculated the inverse distance from the intrusive contacts. Fig. (7) shows the shallow body layer score and C-A and P-A charts as the base for the calculation of the weight of this layer. According to these charts, a weight of 0.12 was obtained for the distance layer of shallow magnetic masses.

4.5.2. Spectrometry Data

Airborne gamma-ray data analysis is a quick and affordable way to map out the distribution of potassium, uranium, and thorium radioactive elements. This technique is often used as a supplementary lithological map, and there is often a strong correlation between radiometric data patterns and fresh rocks. We can gain insight into mineralization by studying these data in conjunction with host rocks [81].

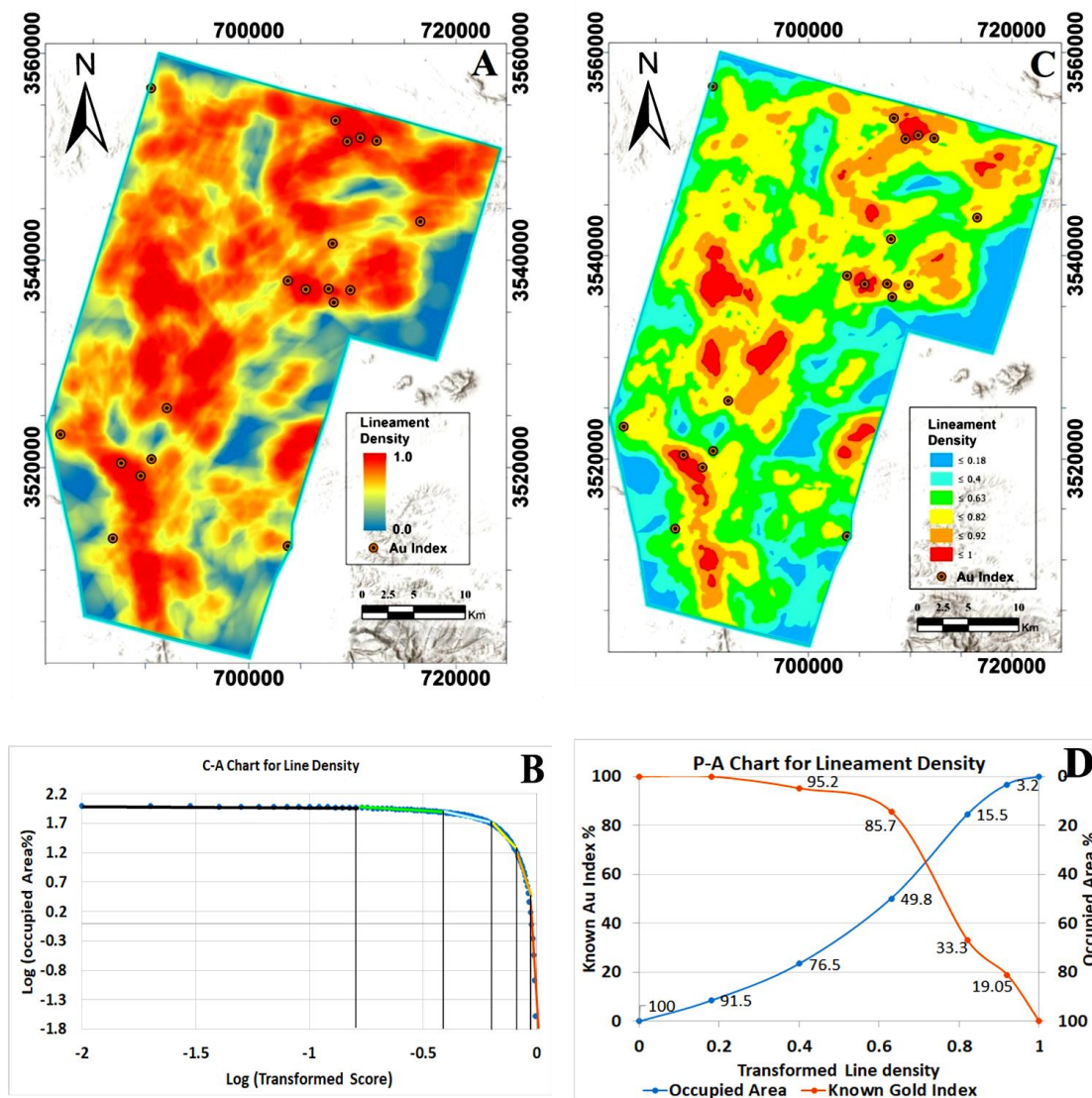


Fig. 6. Maps and charts for Lineament Density Layer -A) Continuous map. -B) C-A Chart of Map (A). -C) Discrete Map Used for Weight Calculation. -D) P-A Chart of Lineament Density map.

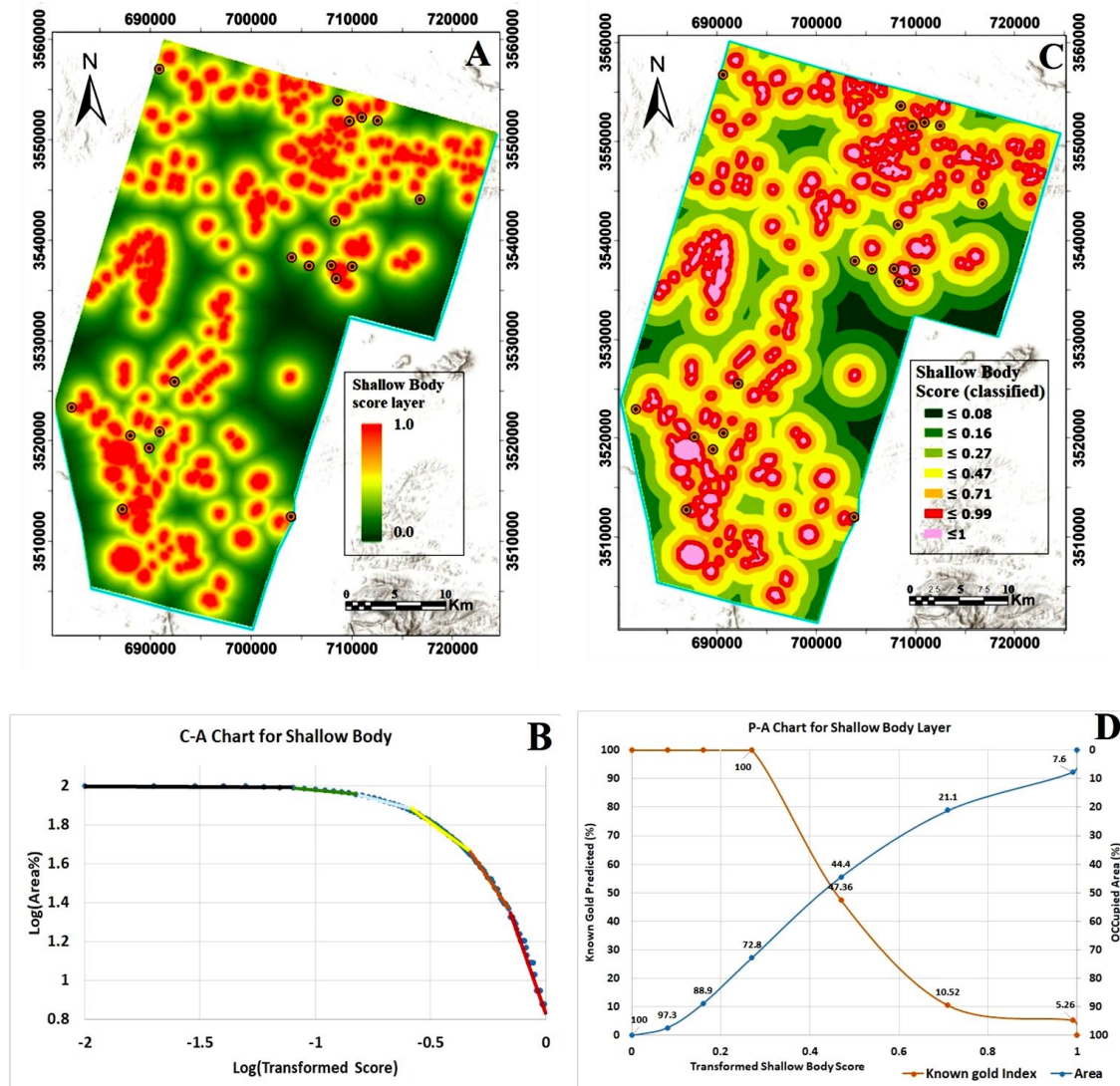


Fig. 7. Maps and charts for Shallow Body Layer. -A) Continuous map. -B) C-A Chart of Map (A). -C) Discrete Map Used for Weight Calculation. -D) P-A Chart of Shallow Body Layer.

Potassium is beneficial as a trace element because its concentration can increase due to potassium metasomatism in K-rich rocks [66], [82]. The K/Th ratio is especially efficient in identifying potassic alteration since potassium (K) is more mobile than thorium (Th) during hydrothermal processes. However, it is essential to note that high K and K/Th values may depend on specific geological contexts [83]. Uranium is often enriched in gold deposits [84], [85].

The weight of radiometric layers was determined by P-A diagrams. Uranium and thorium layers got a negative weight and were not used in the MPM process. The negative weight of these layers can be related to the vast extent of alluvial-covered areas in this area. K and K/Th layers were chosen as proxies due to their relationship with potassic alteration. These layers got weights of 0.12 and 0.16, respectively. The U/Th ratio layer was also selected due to uranium enrichment in gold deposits. This layer has a weight of 0.532. Fig. 8 to 10 shows the selected radiometry proxies map and their related P-A charts.

4.5.3. Electromagnetic data

In this area, airborne frequency domain electromagnetic (AFDEM) maps are available. This technique is commonly utilized for detecting sulfide deposits, which have high to moderate conductivity and

moderate conductivity shear zones for gold. During the operation, a bird flew 30 meters below the Helicopter, and the data was collected at a height 30 m above the ground, using five frequencies of low (875 Hz) to high (33500 Hz). Low-frequency resistivity maps can detect electrical signals from greater depths, while a high-frequency resistance map is sensitive to surface-level signals [68].

Here, we chose a coplanar map with a frequency of 4920 Hz as a proxy for MPM because of the better quality of the map, little surface noise, and better resolution than low-frequency maps. The areas with high resistance in this map have the most convergence with known gold indices in this area, which can be due to the connection of these mineralizations with intrusive masses and siliceous veins. Fig. 11 shows this map and the related C-A and P-A charts. The calculated weight of this resistivity map using the P-A chart was 0.575.

5. Integration of layers

In this study, a logistic function was used to transfer the values of each evidential layer into the range of [0,1], resulting in continuous fuzzy evidential layers without classification. To minimize any bias, the weight of each layer was determined by analyzing the intersection of the P-A

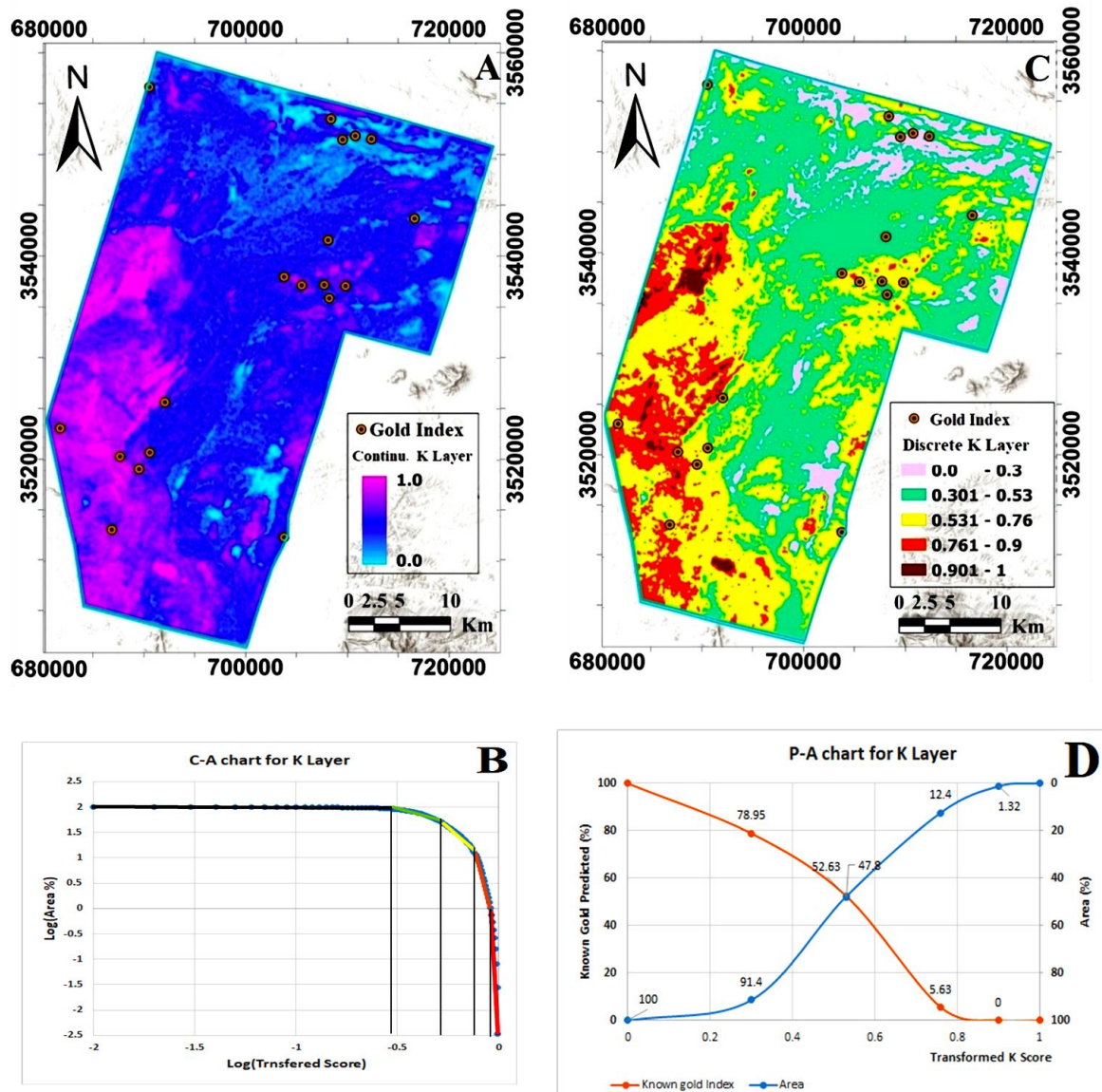


Fig. 8. Maps and charts for K Proxy Layer -A) Continuous map. -B) C-A Chart of Map (A).

-C) Discrete Map Used for Weight Calculation. -D) P-A Chart of K layer.

curves without input from experts. The resulting weights were then integrated to generate a potential map using either the TOPSIS or MIO methods, which will be explored in greater detail below.

5.1. Integration using the TOPSIS method

In 2012, Pazand et al. suggested using the TOPSIS technique for MPM, which was later refined by Abedi et al. in 2015. This method involves preparing various layers and calculating their weights before combining them. TOPSIS has three different approaches, A-TOPSIS, C-TOPSIS, and M-TOPSIS [55], [86]. In this study, we execute TOPSIS calculations using the MATLAB software, in accordance with the formulas expounded in Section 3.3.2 of this paper. The computation of similarity values was carried out for each alternative ("cells" in this context). Subsequently, the MPM scores were generated and the classification of the MPM score map was accomplished using the C-A fractal method. The calculated charts and maps for C-, A-, and M-TOPSIS are visualized in Figures 12 to 14 respectively. Furthermore, the performance of the TOPSIS techniques was assessed through the

generation of P-A charts. According to the results derived from these charts, the C-TOPSIS method demonstrated an ability to identify 75% of gold prospects within 25% of the initial exploration area. Likewise, the A-TOPSIS method exhibited a capability to detect 71% of gold prospects within 29% of the initial exploration area, while the M-TOPSIS method displayed proficiency in identifying 76% of gold prospects within 24% of the initial exploration area.

5.2. Data integration using multi-index overlay (MIO) method

The MIO technique is widely recognized for its capacity to merge data predicated on multiple criteria. It is important to note that this method is essentially synonymous with the weighted average method, which makes it both strong and dependable. Consequently, it can be effectively used for the integration of criteria in order to ascertain optimal alternatives. In order to create the MPM using the MIO method, the evidence layers were integrated in accordance with their respective weights, as determined by equation (11). Figure 15 provides a visual representation of the integrated results emanating from the application

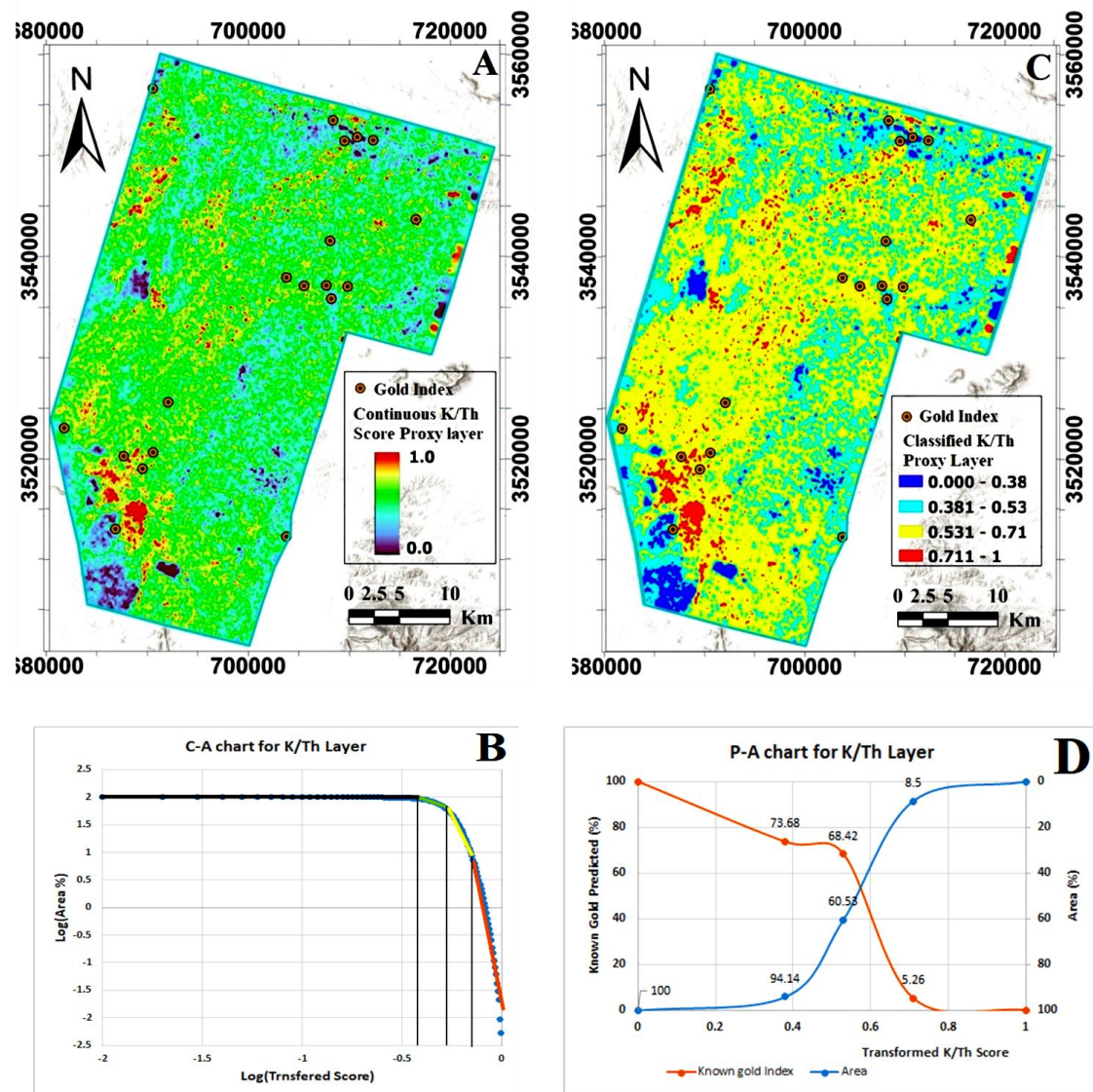


Fig. 9. Maps and charts for K/Th Proxy Layer -A) Continuous map. -B) C-A Chart of Map (A). -C) Discrete Map Used for Weight Calculation. -D) P-A Chart of K/Th layer.

of this method. The P-A chart for this map was also calculated for evaluation of its efficiency. This map can predict 75% of gold deposits within 25% of the study area.

6. Evaluation

In this study, we utilized the MIO and TOPSIS methods to combine various layers. To assess the final models, we employed the P-A and Receiver Operating Characteristic (ROC) charts. The P-A curve's intersection point serves as a benchmark for evaluating the mineral potential model. A more effective model is indicated by a higher intersection point of the two curves, as it identifies known prospects in a smaller portion of the study area [24], [87], [88].

By utilizing the intersection points of the P-A charts as outlined in Fig 16, both integrated models were able to showcase superior quality and efficiency for the layers utilized. In order to obtain a more comprehensive understanding of the efficiency of the TOPSIS and MIO integration methods, a comparative analysis was conducted between

these two and the primary evidential layers. The results of this detailed comparison are visually presented in Figure 16, providing a clear and concise representation of the findings.

In this study, the MIO was able to detect 75% of gold indications over 25% of the area. The TOPSIS model, specifically versions A, C, and M, successfully identified 71%, 75%, and 76% of indications, respectively, but only within 29%, 25%, and 24% of the area. This suggests that the M-TOPSIS method is performing slightly better than the others. The MIO and C-TOPSIS methods were comparable in identifying mineral prospects, while the A-TOPSIS method had the worst results.

The ROC curve is a graph that displays how well a classification model performs at all classification thresholds. It shows two parameters: the True Positive Rate (TPR) and False Positive Rate (FPR) [89], [90]. The ROC curve facilitates a comparative assessment of the model's capacity to accurately discriminate between positive (mineral deposits) and negative (non-mineral deposits) cases [88], [91]. The Area Under the Curve (AUC) is calculated to assess the performance of diverse MPMs, referring to the area beneath the ROC curve. A higher AUC

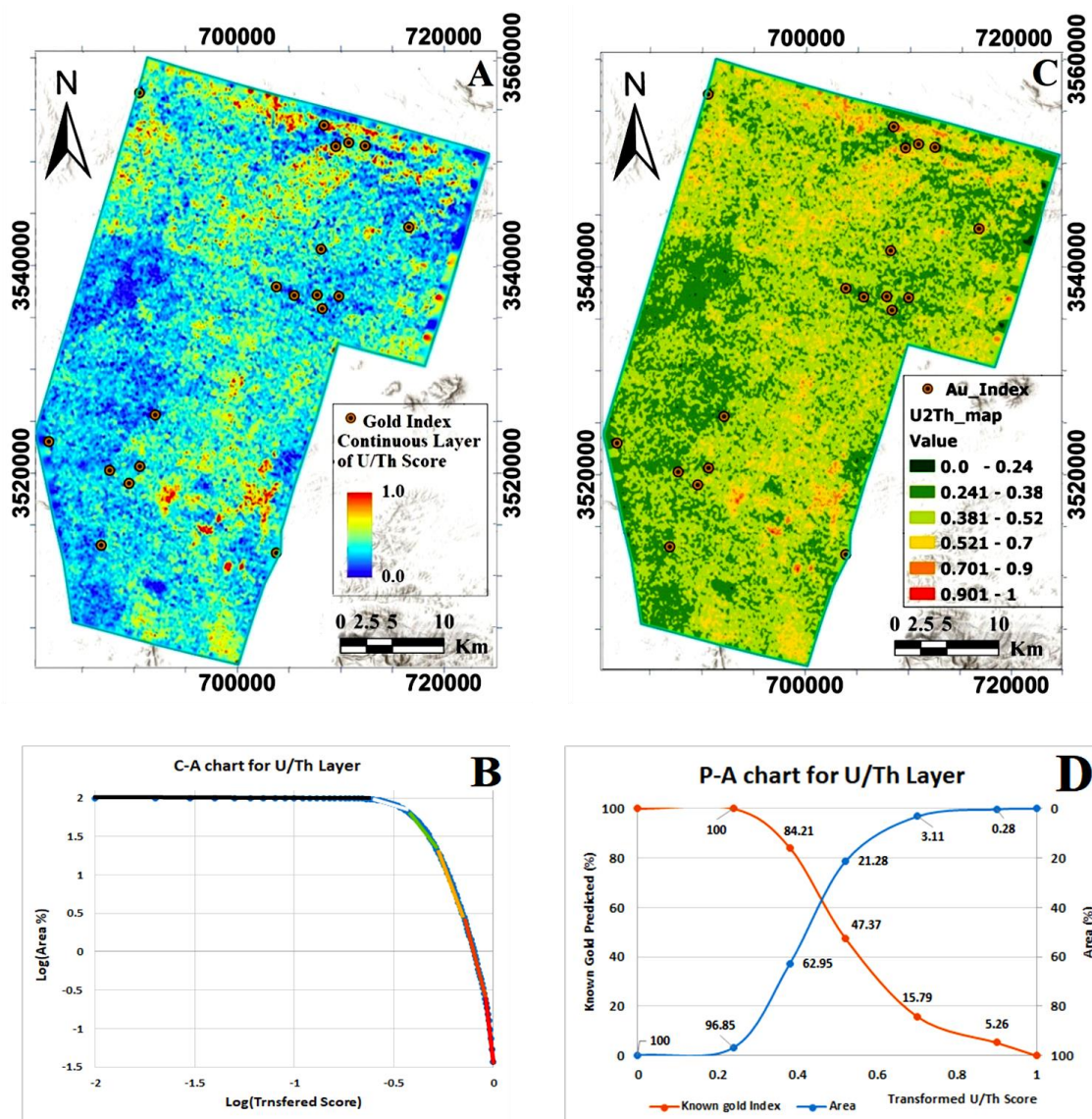


Fig. 10. Maps and charts for U/Th Proxy Layer -A) Continuous Map. -B) C-A Chart of Map (A). -C) Discrete Map Used for Weight Calculation. -D) P-A Chart of U/Th Layer.

value signifies the model's heightened predictive capability, whereas a lower AUC value implies suboptimal performance [87], [92].

However, it is imperative to acknowledge that the choice of negative target locations can influence the outcomes of the ROC analysis. For this study, 19 negative points were selected randomly, and strategically positioned at a considerable distance from gold indexes and intrusive bodies (Fig. 15 A). This selection strategy is employed to ensure the robustness and validity of the ROC analysis results.

Fig. 17 displays the ROC curves and AUC values for integrated results, it shows that the ROC chart of M- and C-TOPSIS are matched. The AUC of the MIO and A-TOPSIS are 0.939 and 0.942 respectively, and that of both M- and C-TOPSIS is 0.967.

7. Discussion

In this study, we adopted a strategy to mitigate the impact of multiple mineral deposits clustered within a confined geographical area. From the total of 21 mineral prospects within the study area, we deliberately selected 19 prospects, each situated at least 500 meters apart from the

others. This selection aimed to enhance the spatial diversity of our sampling points and reduce the potential bias introduced by the proximity of multiple deposits.

To investigate the gold potential within this area, we utilized nine distinct evidence layers encompassing geological data, remote sensing images, geochemical data, and airborne geophysical (Magnetic, radiometric, and electromagnetic) data. In order to facilitate consistent data processing and to avoid classification errors, we applied a sigmoid logistic function to transform the data into a standardized range of [0, 1], and convert them to continuous layers.

For the assignment of weights to these evidence layers, we employed the P-A method, relying on known gold prospects. Importantly, this weighting process was conducted independently of the specific coordinates of the deposit points. Instead, we assessed the efficiency of each layer in identifying gold indications relative to the predefined target area, employing it as the criterion for weighting. For this purpose, it became necessary to utilize different classes of the prospectivity map or target layers, leading us to utilize the C-A fractal model for discretization.

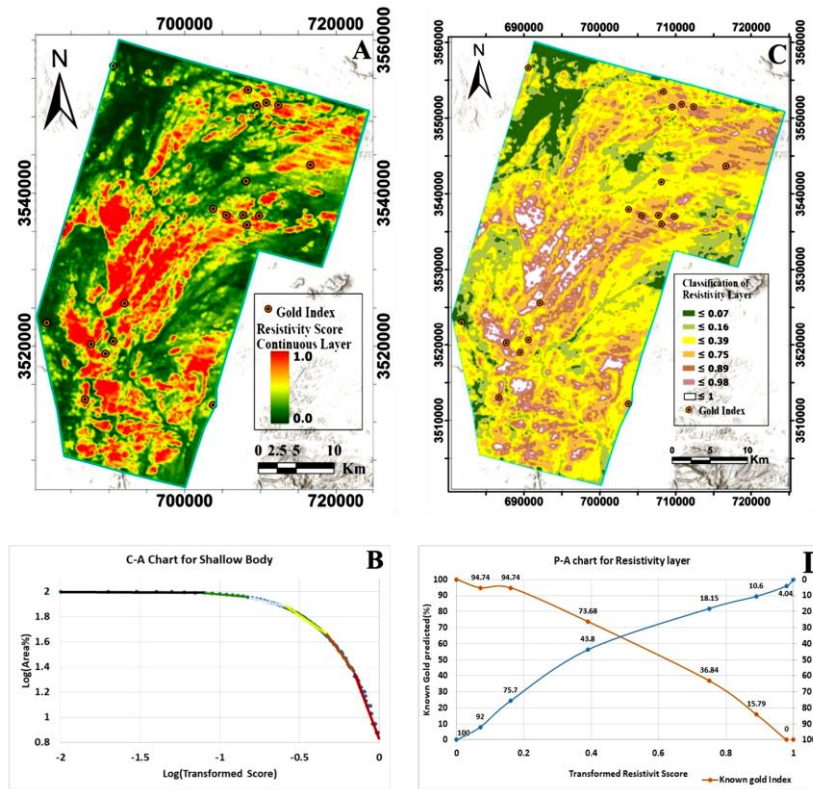


Fig. 11. Maps and charts for Resistivity Layer -A) Continuous Map. -B) C-A Chart of Map (A). -C) Discrete Map Used for Weight Calculation. -D) P-A Chart of Resistivity Layer.

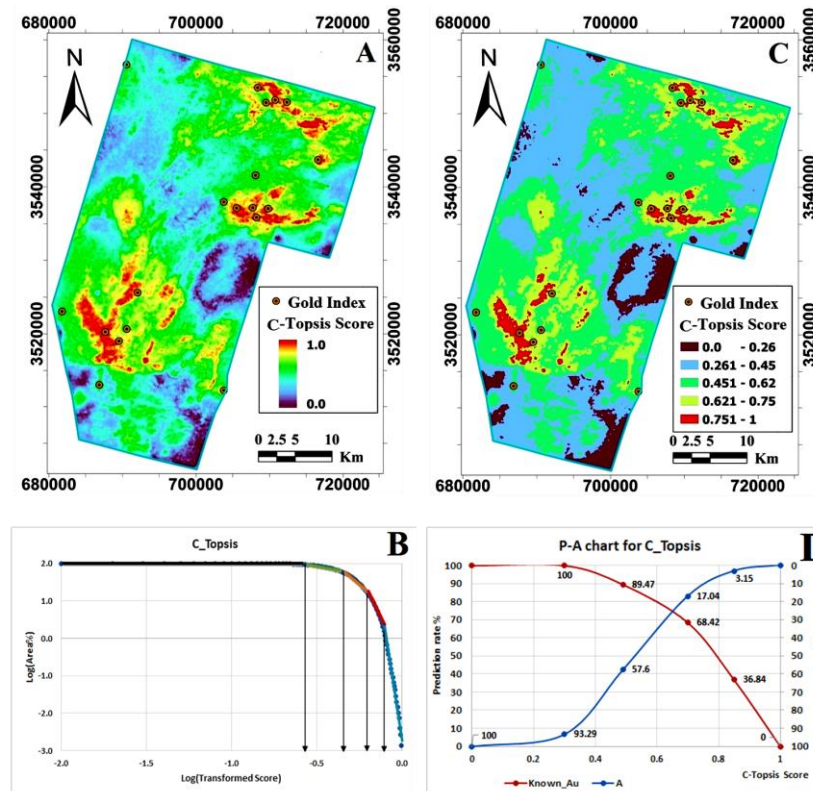


Fig. 12. Maps and charts for MPM using C-TOPSIS method. -A) Continuous map. -B) C-A chart of map (A). -C) Discrete map used for weight calculation. -D) P-A chart of the C-TOPSIS method.

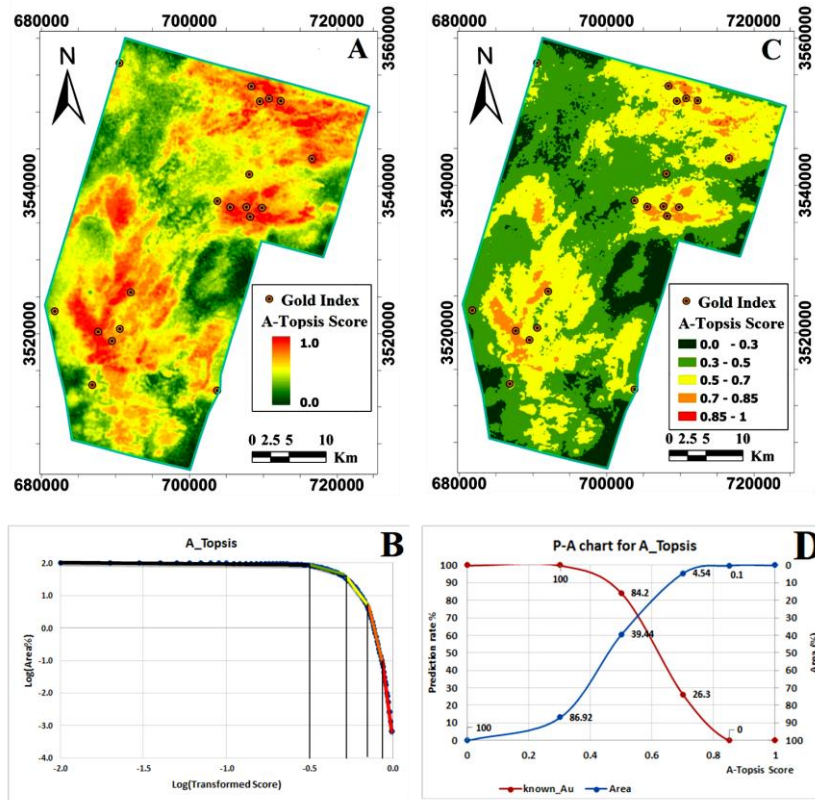


Fig. 13. Maps and charts for MPM Using A-TOPSIS Method. -A) Continuous Map. -B) C-A Chart of Map (A). -C) Discrete Map Used for Weight Calculation. -D) P-A Chart of the A-TOPSIS Method.

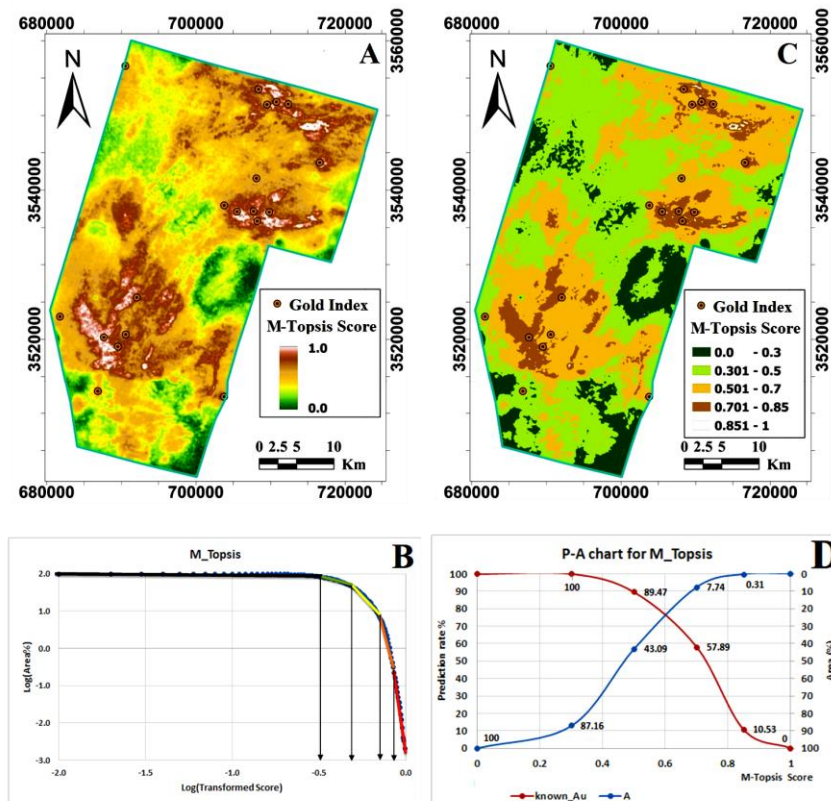


Fig. 14. Maps and charts for MPM Using M-TOPSIS Method. -A) Continuous Map. -B) C-A Chart of Map (A). -C) Discrete Map Used for Weight Calculation. -D) P-A Chart of the M-TOPSIS Method.

The efficacy of decision-making models that rely on data integration is heavily dependent on the quality of the initial models. This study tried to enhance the primary layers used in creating such models. We discovered that some primary layers could be improved with relative ease, while others were more complex and time-consuming. We focused on enhancing the quality of primary layers by reprocessing remote sensing, aerial geophysics, and geochemistry datasets. However, we did not address issues such as errors in geologic maps and inaccurate geochemical results, which necessitated significant time and expenses to rectify.

In this area, the geochemical layer derived from stream sediment data outperforms other primary layers in identifying known gold deposits. It identified 71% of the deposits within 29% of the area, although its performance was better in central and southern parts of the study area. The RS and lineaments layers were ranked second and identified 65% of gold targets within 35% of the area, performing well across the entire area. The resistivity layer obtained from airborne electromagnetic measurements and the ratio U/Th layer were also successful, identifying 64% and 63% of the deposits over 36% and 37% of the study area, respectively. Meanwhile, other layers had a prediction rate between 50% and 60%.

We effectively merged primary layers using the MIO approach and various TOPSIS methods, including C-, M-, and A-TOPSIS. After analyzing the results using P-A charts, we found that all the integrated models except A-TOPSIS showed improved quality and efficacy in utilizing the selected layers. This led to the discovery of more deposits in smaller areas. Based on the intersection points of the P-A chart, both the MIO and C-TOPSIS methods produced comparable results, successfully identifying 75% of the gold deposits within 25% of the study area. It should be noted that the M-TOPSIS method demonstrated a slight superiority over the other methods in identifying mineral

prospects. It detected 76% of gold prospects within 24% of the study area.

In our study, we found that the A-TOPSIS method was not very effective as it only identified 71% of the deposits within only 29% of the study area. This result was similar to the findings of the Geochemistry layer. Upon further investigation, we discovered that A-TOPSIS uses the root of layers weights for *similarity distance* calculation instead of their actual weights (Eq. 15 and 16). This deviation from the main idea of using the weights of layers has weakened the accuracy of this method.

To facilitate the calculation of ROC and AUC, we introduced negative points into the analysis. Despite their influence on the validation results, these negative points were selected at random and located far from gold deposits and intrusive bodies. The computed AUC values for the MIO, A-TOPSIS, C-TOPSIS, and M-TOPSIS methods were found to be 0.939, 0.942, 0.967, and 0.967, respectively. These AUC values significantly diverge from the random guessing value of 0.5, indicating the reliability of the MPM results across all models. Based on these AUC results, the TOPSIS methods outperformed the MIO method, with both C-TOPSIS and M-TOPSIS delivering the most robust results.

Through the analysis of composite maps, it has been determined that there are several points of interest regarding gold prospectivity. Most of these targets are associated with areas that have known mineral deposits. However, these areas are wider and remind the need for further exploration in these areas. Notably, a big anomaly has been detected in the western portion of the area. These findings suggest that these locations may be prime candidates for future exploration programs, for potentials having significant yields. Further geological surveys and assessments will be necessary to fully understand the extent and feasibility of these prospects, paving the way for more in-depth exploration and potentially profitable developments of these prospects in the future.

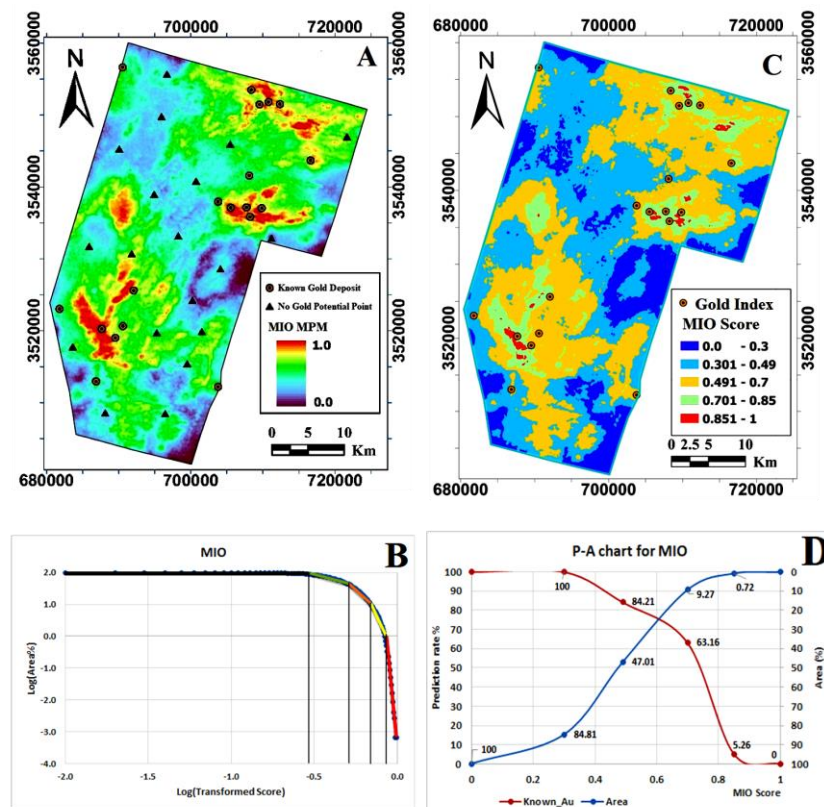


Fig. 15. Maps and charts for MPM Using MIO Method. -A) Continuous Map. -B) C-A Chart of Map (A). -C) Discrete Map Used for Weight Calculation. -D) P-A Chart of MIO MPM Layer.

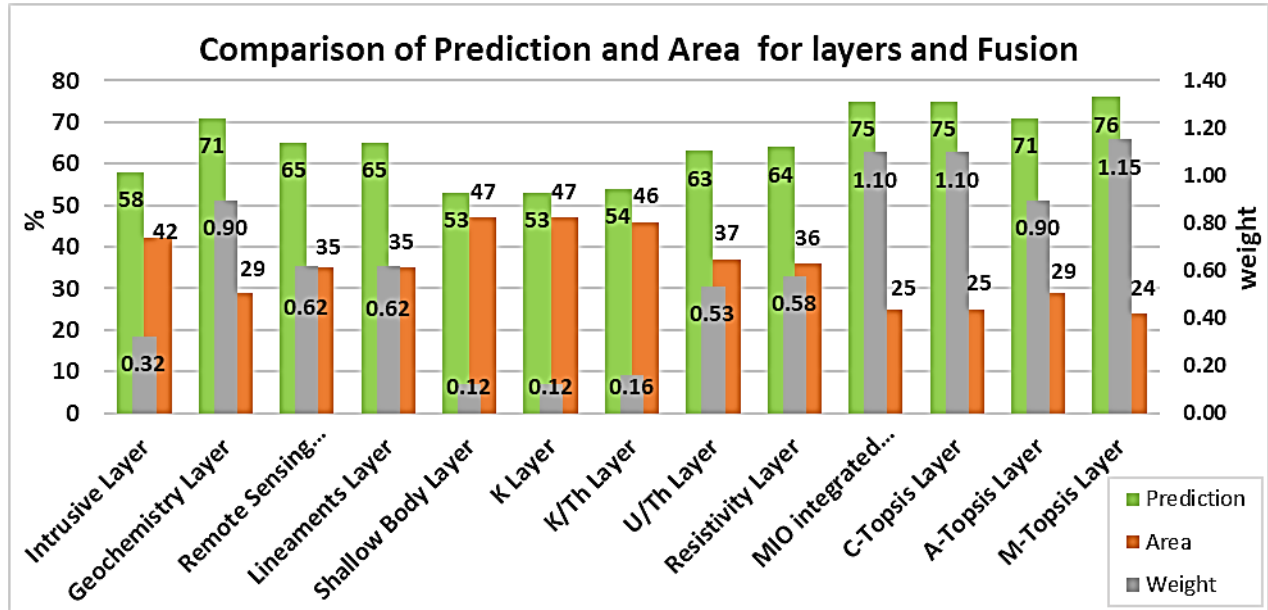


Fig. 16. Prediction, Area, and Calculated Weight for Proxy Layers and the MPMs created using Various TOPSIS (A, C, M) and multi-index overlay integration methods.

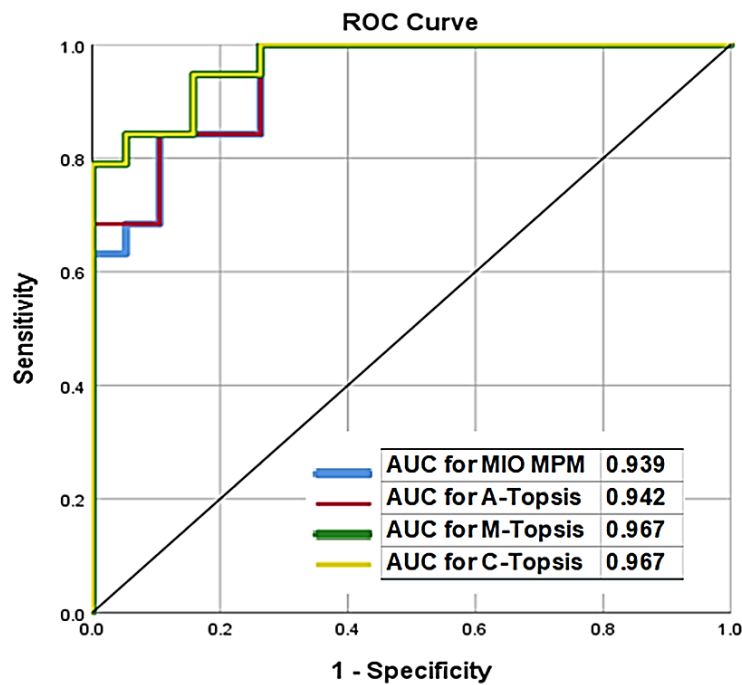


Fig. 17. ROC curve and AUC values for the gold prospectivity map created using Various TOPSIS (A, C, M) and multi-index overlay integration methods.

8. Summary and concluding remarks

In conclusion, this paper aimed to map the gold prospectivity of the Basiran-Mokhtaran region in Iran using four different methods: Multi-Index Overlay (MIO), A-TOPSIS, C-TOPSIS, and M-TOPSIS. These methods are based on the integration of multiple proxies using weights assigned to each criterion. The criteria included geological, geochemical, remote sensing, and geophysical data, which were transformed into continuous values using the sigmoid function. The alternatives were the potential gold zones in the study area. The weights were assigned using the P-A intersection point, which is an efficient technique for determining the optimal weights of layers in prospectivity mapping. The

results of the four methods were compared and validated using known gold occurrences and the ROC charts, which are the commonly used tools for evaluating the performance and accuracy of prediction models.

The main findings of this study were that the four methods produced similar and acceptable results, with high correlation coefficients and accuracy rates. The most prospective areas were located in the north, center, and southwest of the study area, where several gold-bearing structures and mineralization systems were identified. The results also revealed the importance of structural and lithological factors in controlling the gold distribution and potential. Among the four

methods, the M-TOPSIS method performed slightly better than the others, according to both the P-A method and the AUC analysis. However, the differences between the maps generated by the four methods were not significant. On the other hand, the A-TOPSIS method had the lowest prediction rate, and thus was not very successful in this area. This failure was due to the use of the root of the layers' weight in calculating the Similarity distance in this method.

The limitation of this study was the insufficient number of known gold deposits in the study area. Another challenge of this study is the inconsistency of geochemical data in adjacent sheets. Also, the lack of accuracy of geological maps due to the existence of a wide sedimentary coverage was another issue. Future research studies can address these limitations by using more objective and robust methods, collecting more comprehensive and reliable data, and using them in the decision-making process.

This paper contributed to the field of mineral exploration by demonstrating the applicability and effectiveness of the MIO and TOPSIS methods for gold prospectivity mapping. The paper also introduced the P-A method as a promising technique for assigning weights to different criteria in prospectivity mapping. It also provided valuable information and insights for the exploration and development of gold resources in the Basiran-Mokhtaran region and other similar areas.

Acknowledgment

The authors express their sincere gratitude to the Geological Survey of Iran (GSI) for generously supplying the essential datasets employed in this research. Mehdi Azadi is also thanked for editing the final version of the manuscript.

REFERENCES

- [1] C. Zheng et al., "Mineral prospectivity mapping based on Support vector machine and Random Forest algorithm – A case study from Ashele copper–zinc deposit, Xinjiang, NW China," *Ore Geol Rev*, vol. 159, p. 105567, Aug. 2023, doi: 10.1016/j.oregeorev.2023.105567.
- [2] R. S. Davies, D. I. Groves, A. Trench, and M. Dentith, "Towards producing mineral resource-potential maps within a mineral systems framework, with emphasis on Australian orogenic gold systems," *Ore Geol Rev*, vol. 119, no. January, p. 103369, 2020, doi: 10.1016/j.oregeorev.2020.103369.
- [3] S. A. A. S. Mirzabozorg and M. Abedi, "Recognition of mineralization-related anomaly patterns through an autoencoder neural network for mineral exploration targeting," *Applied Geochemistry*, vol. 158, p. 105807, Nov. 2023, doi: 10.1016/j.apgeochem.2023.105807.
- [4] S. Sahoo, A. Singh, S. Biswas, and S. P. Sharma, "3D Subsurface Characterization of Banded Iron Formation Mineralization using Large-Scale Gravity Data: A Case Study in Parts of Bharatpur, Dausa and Karauli Districts of Rajasthan, India," *Natural Resources Research*, vol. 30, no. 5, pp. 3121–3138, Oct. 2021, doi: 10.1007/s11053-021-09880-y.
- [5] Z. Wang, R. Zuo, and L. Jing, "Fusion of Geochemical and Remote-Sensing Data for Lithological Mapping Using Random Forest Metric Learning," *Math Geosci*, vol. 53, no. 6, pp. 1125–1145, Aug. 2021, doi: 10.1007/s11004-020-09897-8.
- [6] Q. Cheng, "Singularity theory and methods for mapping geochemical anomalies caused by buried sources and for predicting undiscovered mineral deposits in covered areas," *J Geochem Explor*, vol. 122, pp. 55–70, 2012, doi: 10.1016/j.gexplo.2012.07.007.
- [7] Y. Xiong, R. Zuo, and E. J. M. Carranza, "Mapping mineral prospectivity through big data analytics and a deep learning algorithm," *Ore Geol Rev*, vol. 102, no. September, pp. 811–817, 2018, doi: 10.1016/j.oregeorev.2018.10.006.
- [8] M. Yousefi, O. P. Kreuzer, V. Nykänen, and J. M. A. Hronsky, "Exploration information systems – A proposal for the future use of GIS in mineral exploration targeting," *Ore Geol Rev*, vol. 111, no. July, 2019, doi: 10.1016/j.oregeorev.2019.103005.
- [9] Z. PENGDA, C. QIUMING, and X. QINGLIN, "Quantitative Prediction for Deep Mineral Exploration," *Journal of China University of Geosciences*, vol. 19, no. 4, pp. 309–318, Aug. 2008, doi: 10.1016/S1002-0705(08)60063-1.
- [10] E. J. M. Carranza, *Geochemical Anomaly and Mineral Prospectivity Mapping in GIS*, no. November. 2009.
- [11] M. Yousefi, E. J. M. Carranza, O. P. Kreuzer, V. Nykänen, J. M. A. Hronsky, and M. J. Mihalasky, "Data analysis methods for prospectivity modelling as applied to mineral exploration targeting: State-of-the-art and outlook," *J Geochem Explor*, vol. 229, no. April, 2021, doi: 10.1016/j.gexplo.2021.106839.
- [12] A. Shabani, M. Ziaii, M. Monfared, A. Shirazy, and A. Shirazi, "Multi-Dimensional Data Fusion for Mineral Prospectivity Mapping (MPM) Using Fuzzy-AHP Decision-Making Method, Kodegan-Basiran Region, East Iran," *Minerals*, vol. 12, no. 12, p. 1629, Dec. 2022, doi: 10.3390/min12121629.
- [13] B. Boadi, P. V. Sunder Raju, and D. D. Wemegah, "Analysing multi-index overlay and fuzzy logic models for lode-gold prospectivity mapping in the Ahafo gold district – Southwestern Ghana," *Ore Geol Rev*, vol. 148, p. 105059, Sep. 2022, doi: 10.1016/j.oregeorev.2022.105059.
- [14] S. Riahi, A. Bahroudi, M. Abedi, D. R. Lentz, and S. Aslani, "Application of data-driven multi-index overlay and BWM-MOORA MCDM methods in mineral prospectivity mapping of porphyry Cu mineralization," *J Appl Geophy*, vol. 213, p. 105025, Jun. 2023, doi: 10.1016/j.jappgeo.2023.105025.
- [15] D. I. Groves, M. Santosh, and L. Zhang, "A scale-integrated exploration model for orogenic gold deposits based on a mineral system approach," *Geoscience Frontiers*, vol. 11, no. 3, pp. 719–738, 2020, doi: 10.1016/j.gsf.2019.12.007.
- [16] M. Yousefi and V. Nykänen, "Introduction to the special issue: GIS-based mineral potential targeting," *Journal of African Earth Sciences*, vol. 128, pp. 1–4, Apr. 2017, doi: 10.1016/j.jafrearsci.2017.02.023.
- [17] A. Aryafar and B. Roshanravan, "Improved index overlay mineral potential modeling in brown- and green-fields exploration using geochemical, geological and remote sensing data," *Earth Sci Inform*, vol. 13, no. 4, pp. 1275–1291, 2020, doi: 10.1007/s12145-020-00509-x.
- [18] G. F. Bonham-Carter, "Geographic information systems for geoscientists: Modelling with GIS," *Comput Geosci*, vol. 21, no. 9, pp. 1110–1112, 1995, doi: 10.1016/0098-3004(95)90019-5.
- [19] M. Abedi, S. B. Mostafavi Kashani, G. H. Norouzi, and M. Yousefi, "A deposit scale mineral prospectivity analysis: A comparison of various knowledge-driven approaches for porphyry copper targeting in Seridune, Iran," *Journal of African Earth Sciences*, vol. 128, pp. 127–146, 2017, doi: 10.1016/j.jafrearsci.2016.09.028.
- [20] E. J. M. Carranza, "Geocomputation of mineral exploration targets," *Comput Geosci*, vol. 37, no. 12, pp. 1907–1916, Dec. 2011.
- [21] M. Yousefi and E. J. M. Carranza, "Geometric average of spatial evidence data layers: A GIS-based multi-criteria decision-making approach to mineral prospectivity mapping," *Comput Geosci*, vol. 83, pp. 72–79, Oct. 2015, doi: 10.1016/j.cageo.2015.07.006.
- [22] M. Krstić, S. Tadić, M. Kovač, V. Roso, and S. Zečević, "A Novel Hybrid MCDM Model for the Evaluation of Sustainable Last Mile Solutions," *Math Probl Eng*, vol. 2021, pp. 1–17, Oct. 2021, doi: 10.1155/2021/5969788.
- [23] V. Nykänen and V. J. Ojala, "Spatial analysis techniques as successful mineral-potential mapping tools for orogenic gold deposits in the northern Fennoscandian shield, Finland," *Natural Resources Research*, vol. 16, no. 2, pp. 85–92, Jun. 2007, doi: 10.1007/S11053-007-9046-5.
- [24] S. Riahi, A. Bahroudi, M. Abedi, S. Aslani, and D. R. Lentz, "Evidential data integration to produce porphyry Cu prospectivity map, using a combination of knowledge and data - driven methods," *Geophys Prospect*, vol. 70, no. 2, pp. 421–437, Feb. 2022, doi: 10.1111/1365-2478.13169.
- [25] M. Alavi, "Sedimentary and structural characteristics of the paleo-Tethys remnants in northeastern Iran," *Geol Soc Am Bull*, vol. 103, pp. 983–992, 1991.
- [26] A. Aghanabati, *Geology of Iran*. Tehran: Geological Survey of Iran, 2005.

- [27] V. E. Camp, R. J. Griffis, G. R. Camp V, V. E. Camp, and R. J. Griffis, "Character, genesis and tectonic setting of igneous rocks in the Sistan suture zone, eastern Iran," *Lithos*, vol. 15, no. 3, pp. 221–239, 1982, doi: 10.1016/0024-4937(82)90014-7.
- [28] R. Tirrul, I. R. Bell, R. J. Griffis, and V. E. Camp, "The Sistan suture zone of eastern Iran," *GSA Bulletin*, vol. 94, no. 1, pp. 134–150, Jan. 1983, doi: 10.1130/0016-7606(1983)94<134:TSSZOE>2.0.CO;2.
- [29] B. Meyer and K. Le Dortz, "Strike-slip kinematics in Central and Eastern Iran: Estimating fault slip-rates averaged over the Holocene," *Tectonics*, vol. 26, no. 5, p. n/a-n/a, Oct. 2007, doi: 10.1029/2006TC002073.
- [30] J. Jackson and D. McKenzie, "Active tectonics of the Alpine-Himalayan Belt between western Turkey and Pakistan," *Geophys J Int*, vol. 77, no. 1, pp. 185–264, Apr. 1984, doi: 10.1111/j.1365-246X.1984.tb01931.x.
- [31] M. Ghorbani, Geological Setting and Crustal Structure of Iran. 2021. doi: 10.1007/978-3-030-71109-2_1.
- [32] R. Walker and J. Jackson, "Active tectonics and late Cenozoic strain distribution in central and eastern Iran," *Tectonics*, vol. 23, no. 5, p. n/a-n/a, Oct. 2004, doi: 10.1029/2003TC001529.
- [33] S. Samimi, E. Gholami, M. M. Khatib, S. Madanipour, and F. Lisker, "Transpression and Exhumation of Granitoid Plutons along the Northern Part of the Nehbandan Fault System in the Sistan Suture Zone, Eastern Iran," *Geotectonics*, vol. 54, no. 1, pp. 130–144, Jan. 2020, doi: 10.1134/S0016852120010124.
- [34] M. Delaloye and J. Desmons, "Ophiolites and melange terranes in Iran: A geochronological study and its paleotectonic implications," *Tectonophysics*, vol. 68, no. 1–2, pp. 83–111, Sep. 1980, doi: 10.1016/0040-1951(80)90009-8.
- [35] Z. Khajehmiri, M. R. Shayestehfar, and H. Moeinzadeh, "Using Spectral Angle Method to Detect Alterations in Sheets of Mokhtaran and Sarchahshur," vol. 1, no. 1, pp. 11–22, 2018.
- [36] J. Golonka, "Plate tectonic evolution of the southern margin of Eurasia in the Mesozoic and Cenozoic," *Tectonophysics*, vol. 381, no. 1–4, pp. 235–273, Mar. 2004, doi: 10.1016/j.tecto.2002.06.004.
- [37] D. Jung, J. Keller, R. Khorasani, Chr. Marcks, A. Baumann, and P. Horn, "Petrology of the Tertiary Magmatic Activity in the Northern Lut Area, East Iran," *Neues Jahrb Geol Palaontol Abh*, vol. 168, no. 2–3, pp. 417–467, Jun. 1984, doi: 10.1127/njgpa/168/1984/417.
- [38] A. Malekzadeh Shafaroudi, M. H. Karimpour, and C. R. Stern, "The Khopik porphyry copper prospect, Lut Block, Eastern Iran: Geology, alteration and mineralization, fluid inclusion, and oxygen isotope studies," *Ore Geol Rev*, vol. 65, pp. 522–544, 2015, doi: https://doi.org/10.1016/j.oregeorev.2014.04.015.
- [39] B. A. Tarkian M, Lotfi M, "Tectonic, magmatism and the formation of mineral deposits in the central Lut, east Iran, Ministry of mines and metals, GSI, Geodynamic project (geotraverse) in Iran, Geological Survey of Iran," Report 51, Iran, 1983.
- [40] A. Behrouzi, N. K. Nazer, F. Ezattian, M. Davari, and I. Eftekharneshad, *Geological Map Of Iran - 1:100,000 Series, Sheet 7754 - Basiran*. Tehran: Geological Survey of Iran, 1992.
- [41] H. Movahhed, M. H. Emami, J. Eftekharneshad, and J. Stocklin, *Geological Map Of Iran - 1:100,000 Series, Sheet 7854 - Mokhtaran*. Tehran: Geological Survey of Iran, 1978.
- [42] R. Arjmandzadeh, S. Alirezaei, and A. Almasi, "Tectonomagmatic reconstruction of the Upper Mesozoic–Cenozoic Neotethyan arcs in the Lut block, East Iran: a review and synthesis," *Turkish Journal of Earth Sciences*, vol. 31, no. 6, pp. 520–544, 2022, doi: 10.55730/1300-0985.1818.
- [43] S. Samiee, M. H. Karimpour, M. Ghaderi, M. R. Haidarian Shahri, U. Klötzli, and J. F. Santos, "Petrogenesis of subvolcanic rocks from the Khunik prospecting area, south of Birjand, Iran: Geochemical, Sr–Nd isotopic and U–Pb zircon constraints," *J Asian Earth Sci*, vol. 115, pp. 170–182, 2016, doi: https://doi.org/10.1016/j.jseas.2015.09.023.
- [44] N. Vafaei, R. A. Ribeiro, and L. M. Camarinha-Matos, "Normalization Techniques for Multi-Criteria Decision Making: Analytical Hierarchy Process Case Study," 2016, pp. 261–269. doi: 10.1007/978-3-319-31165-4_26.
- [45] M. Yousefi and E. J. M. Carranza, "Fuzzification of continuous-value spatial evidence for mineral prospectivity mapping," *Comput Geosci*, vol. 74, pp. 97–109, 2015, doi: 10.1016/j.cageo.2014.10.014.
- [46] A. Jahan and K. L. Edwards, "A state-of-the-art survey on the influence of normalization techniques in ranking: Improving the materials selection process in engineering design," *Materials & Design* (1980-2015), vol. 65, pp. 335–342, 2015, doi: https://doi.org/10.1016/j.matdes.2014.09.022.
- [47] E. D. Forson et al., "Data-driven multi-index overlay gold prospectivity mapping using geophysical and remote sensing datasets," *Journal of African Earth Sciences*, vol. 190, p. 104504, Jun. 2022, doi: 10.1016/j.jafrearsci.2022.104504.
- [48] M. Yousefi, S. Yousefi, and A. Kamkar-Rouhani, "Recognition coefficient of spatial geological features, an approach to facilitate criteria weighting for mineral exploration targeting," *IJMGE*, vol. 57, no. 3, pp. 251–258, 2023, doi: 10.22059/IJMGE.2023.355380.595037.
- [49] P. Afzal, R. A. Asl, A. Adib, and A. B. Yasrebi, "Application of Fractal Modelling for Cu Mineralisation Reconnaissance by ASTER Multispectral and Stream Sediment Data in Khoshname Area, NW Iran," *Journal of the Indian Society of Remote Sensing*, vol. 43, no. 1, pp. 121–132, 2015, doi: 10.1007/s12524-014-0384-6.
- [50] M. Yousefi and E. J. M. Carranza, "Prediction-area (P-A) plot and C-A fractal analysis to classify and evaluate evidential maps for mineral prospectivity modeling," *Comput Geosci*, vol. 79, pp. 69–81, 2015, doi: 10.1016/j.cageo.2015.03.007.
- [51] R. Ghezlbash, A. Maghsoudi, A. Bigdeli, and E. J. M. Carranza, "Regional-Scale Mineral Prospectivity Mapping: Support Vector Machines and an Improved Data-Driven Multi-criteria Decision-Making Technique," *Natural Resources Research*, vol. 30, no. 3, pp. 1977–2005, 2021, doi: 10.1007/s11053-021-09842-4.
- [52] M. Yousefi and J. M. A. Hronsky, "Translation of the function of hydrothermal mineralization-related focused fluid flux into a mappable exploration criterion for mineral exploration targeting," *Applied Geochemistry*, vol. 149, no. October 2022, p. 105561, 2023, doi: 10.1016/j.apgeochem.2023.105561.
- [53] M. Parsa, A. Maghsoudi, M. Yousefi, and M. Sadeghi, "Recognition of significant multi-element geochemical signatures of porphyry Cu deposits in Noghdoz area, NW Iran," *J Geochem Explor*, vol. 165, pp. 111–124, 2016, doi: 10.1016/j.gexplo.2016.03.009.
- [54] K. Yoon, "A Reconciliation Among Discrete Compromise Solutions," *Journal of the Operational Research Society*, vol. 38, no. 3, pp. 277–286, Mar. 1987, doi: 10.1057/jors.1987.44.
- [55] M. Abedi and G.-H. Norouzi, "A general framework of TOPSIS method for integration of airborne geophysics, satellite imagery, geochemical and geological data," *International Journal of Applied Earth Observation and Geoinformation*, vol. 46, pp. 31–44, 2016, doi: https://doi.org/10.1016/j.jag.2015.11.016.
- [56] F. Feizi, A. Karbalaee-Ramezani, and H. Tusi, "Mineral Potential Mapping Via TOPSIS with Hybrid AHP–Shannon Entropy Weighting of Evidence: A Case Study for Porphyry-Cu, Farmahin Area, Markazi Province, Iran," *Natural Resources Research*, vol. 26, no. 4, pp. 553–570, Oct. 2017, doi: 10.1007/s11053-017-9338-3.
- [57] E. K. Zavadskas, A. Mardani, Z. Turskis, A. Jusoh, and K. M. Nor, "Development of TOPSIS Method to Solve Complicated Decision-Making Problems - An Overview on Developments from 2000 to 2015," vol. 15, no. 3, 2016. doi: 10.1142/S0219622016300019.
- [58] H. Deng, C.-H. Yeh, and R. J. Willis, "Inter-company comparison using modified TOPSIS with objective weights," *Comput Oper Res*, vol. 27, no. 10, pp. 963–973, Sep. 2000, doi: 10.1016/S0305-0548(99)00069-6.
- [59] H. Bahrami, S. Homayouni, A. Safari, S. Mirzaei, M. Mahdianpari, and O. Reisi-Gahrouei, "Deep learning-based estimation of crop biophysical parameters using multi-source and multi-temporal remote sensing observations," *Agronomy*, vol. 11, no. 7, 2021, doi: 10.3390/agronomy11071363.
- [60] V. Lisitsin, "Spatial data analysis of mineral deposit point patterns: Applications to exploration targeting," *Ore Geol Rev*, vol. 71, pp. 861–881, 2015, doi: 10.1016/j.oregeorev.2015.05.019.
- [61] S. Ghasemzadeh, A. Maghsoudi, M. Yousefi, and M. J. Mihalasky, "Stream sediment geochemical data analysis for district-scale mineral

- exploration targeting: Measuring the performance of the spatial U-statistic and C-A fractal modeling," *Ore Geol Rev*, vol. 113, p. 103115, Oct. 2019, doi: 10.1016/j.oregeorev.2019.103115.
- [62] M. E. Doherty, K. Arndt, Z. Chang, K. Kelley, and O. Lavin, "Stream sediment geochemistry in mineral exploration: a review of fine-fraction, clay-fraction, bulk leach gold, heavy mineral concentrate and indicator mineral chemistry," *Geochemistry: Exploration, Environment, Analysis*, Jun. 2023, doi: 10.1144/geochem2022-039.
- [63] A. Saydi, M. Abedi, A. Bahroudi, and H. Ferdowsi, "Geochemical prospectivity of Cu-mineralization through concentration-number fractal modeling and prediction-area plot: a case study in East Iran," *International Journal of Mining and Geo-Engineering*, vol. 57, no. 2, pp. 159–169, Jun. 2023, doi: 10.22059/IJMGE.2022.347447.594993.
- [64] A. B. Pour and M. Hashim, "Hydrothermal alteration mapping from Landsat-8 data, Sar Cheshmeh copper mining district, south-eastern Islamic Republic of Iran," *Journal of Taibah University for Science*, vol. 9, no. 2, pp. 155–166, 2015, doi: 10.1016/j.jtusci.2014.11.008.
- [65] E. Jude Steven, A. Suleiman, A. Asema Ibrahim, and U. Mohammed Umar, "Predictive Mapping of the Mineral Potential Using Geophysical and Remote Sensing Datasets in Parts of Federal Capital Territory, Abuja, North-Central Nigeria," *Earth Sciences*, vol. 9, no. 5, p. 148, 2020, doi: 10.11648/j.earth.20200905.12.
- [66] F. Mami, S. Barak, M. Abedi, and S. Yousefi, "Gold prospectivity mapping through generation and integration of geophysical, geochemical, remote sensing, and geological evidence layers in Saqez area, NW Iran", doi: 10.22059/IJMGE.2023.358626.595062.
- [67] M. Airo, "Geophysical signatures of deposits," *Geological Survey of Finland*, vol. 58, no. 58, pp. 9–70, 2015.
- [68] A. M. SILVA, A. C. B. PIRES, A. MCCAFFERTY, R. A. V. DE MORAES, and H. XIA, "Application of airborne geophysical data to mineral exploration in the uneven exposed terrains of the Rio das Velhas greenstone belt," *Revista Brasileira de Geociências*, vol. 33, no. 2, pp. 17–28, Jun. 2003, doi: 10.25249/0375-7536.200333S21728.
- [69] A. A. El-Raouf, F. Doğru, K. Abdelrahman, M. S. Fnais, A. El Manharawy, and O. Amer, "Using Airborne Geophysical and Geochemical Methods to Map Structures and Their Related Gold Mineralization," *Minerals*, vol. 13, no. 2, p. 237, Feb. 2023, doi: 10.3390/min13020237.
- [70] A. M. Silva*, C. G. de Oliveira, G. C. Marques, and A. C. B. Pires, "Relationship between airborne geophysical signatures and hydrothermal rocks with Cu-Au mineralization in the Mara Rosa Magmatic Arc, Central Brazil," in *10th International Congress of the Brazilian Geophysical Society & EXPOGEF 2007*, Rio de Janeiro, Brazil, 19-23 November 2007, Brazilian Geophysical Society, Nov. 2007, pp. 999–1003. doi: 10.1190/sbgf2007-192.
- [71] J. Torppa, V. Nykänen, and F. Molnár, "Unsupervised clustering and empirical fuzzy memberships for mineral prospectivity modelling," *Ore Geol Rev*, vol. 107, no. January, pp. 58–71, 2019, doi: 10.1016/j.oregeorev.2019.02.007.
- [72] T. Sun, F. Chen, L. Zhong, W. Liu, and Y. Wang, "GIS-based mineral prospectivity mapping using machine learning methods: A case study from Tongling ore district, eastern China," *Ore Geol Rev*, vol. 109, no. April, pp. 26–49, Jun. 2019, doi: 10.1016/j.oregeorev.2019.04.003.
- [73] G. Partington, "Developing models using GIS to assess geological and economic risk: An example from VMS copper gold mineral exploration in Oman," *Ore Geol Rev*, vol. 38, no. 3, pp. 197–207, Nov. 2010, doi: 10.1016/j.oregeorev.2010.02.002.
- [74] M. Mohammadpour, A. Bahroudi, and M. Abedi, "Automatic Lineament Extraction Method in Mineral Exploration Using CANNY Algorithm and Hough Transform," *Geotectonics*, vol. 54, no. 3, pp. 366–382, 2020, doi: 10.1134/S00168521200300085.
- [75] S. G. Hagemann, V. A. Litsitsin, and D. L. Huston, "Mineral system analysis: Quo vadis," *Ore Geol Rev*, vol. 76, pp. 504–522, Jul. 2016.
- [76] J. P. Richards, T. Spell, E. Rameh, A. Raziq, and T. Fletcher, "High Sr/Y magmas reflect arc maturity, high magmatic water content, and porphyry Cu ± Mo ± Au potential: Examples from the tethyan arcs of central and eastern Iran and Western Pakistan," *Economic Geology*, vol. 107, no. 2, pp. 295–332, 2012, doi: 10.2113/econgeo.107.2.295.
- [77] M. Billa et al., "Predicting gold-rich epithermal and porphyry systems in the central Andes with a continental-scale metallogenic GIS," *Ore Geol Rev*, vol. 25, no. 1–2, pp. 39–67, 2004, doi: 10.1016/j.oregeorev.2004.01.002.
- [78] R. H. Sillitoe, "Porphyry copper systems," *Economic Geology*, vol. 105, no. 1, pp. 3–41, 2010, doi: 10.2113/gsecongeo.105.1.3.
- [79] N. T. T. Hang, D. D. Thanh, and L. H. Minh, "Application of directional derivative method to determine boundary of magnetic sources by total magnetic anomalies," *VIETNAM JOURNAL OF EARTH SCIENCES*, vol. 39, no. 4, Sep. 2017, doi: 10.15625/0866-7187/39/4/10731.
- [80] L. Pham Thanh et al., "Determination of subsurface lineaments in the Hoang Sa islands using enhanced methods of gravity total horizontal gradient," *Vietnam Journal of Earth Sciences*, Mar. 2022, doi: 10.15625/2615-9783/17013.
- [81] P. J. Gunn, B. R. S. Minty, and P. R. Milligan, "The-Airborne-Gamma-Ray-Spectrometric-Response-Over-Arid-Australian-Terranes," *Fourth Decennial International Conference on Mineral Exploration*, pp. 733–740, 1997.
- [82] B. L. Dickson and K. M. Scott, "Interpretation of aerial gamma-ray survey - adding geochemical factors," *AGSO J Aust Geol Geophys*, vol. 17, no. 2, pp. 187–200, 1997.
- [83] S. H. Abd El Nabi, "Role of γ -ray spectrometry in detecting potassic alteration associated with Um Ba'anib granitic gneiss and metasediments, G. Meatiq area, Central Eastern Desert, Egypt," *Arabian Journal of Geosciences*, vol. 6, no. 4, pp. 1249–1261, Apr. 2013, doi: 10.1007/s12517-011-0378-4.
- [84] I. C. Okeyode, O. T. Olurin, S. A. Ganiyu, and J. A. Olowofela, "High resolution airborne radiometric and magnetic studies of ilesha and its environs, southwestern Nigeria," *Materials and Geoenvironment*, vol. 66, no. 1, pp. 51–73, Mar. 2019, doi: 10.2478/rmzmag-2018-0020.
- [85] D. B. Hoover and H. A. Pierce, "Annotated bibliography of gamma-ray methods applied to gold exploration," 1990.
- [86] F. Feizi, A. Karbalaei-Ramezani, and H. Tusi, "Mineral Potential Mapping Via TOPSIS with Hybrid AHP–Shannon Entropy Weighting of Evidence: A Case Study for Porphyry-Cu, Farmahin Area, Markazi Province, Iran," *Natural Resources Research*, vol. 26, no. 4, pp. 553–570, Oct. 2017, doi: 10.1007/s11053-017-9338-3.
- [87] Y. Ma, J. Zhao, Y. Sui, S. Liao, and Z. Zhang, "Application of knowledge-driven methods for mineral prospectivity mapping of polymetallic sulfide deposits in the southwest Indian ridge between 46° and 52°E," *Minerals*, vol. 10, no. 11, pp. 1–18, 2020, doi: 10.3390/min10110970.
- [88] H. Rahimi, M. Abedi, M. Yousefi, A. Bahroudi, and G. R. Elyasi, "Supervised mineral exploration targeting and the challenges with the selection of deposit and non-deposit sites thereof," *Applied Geochemistry*, vol. 128, May 2021, doi: 10.1016/j.apgeochem.2021.104940.
- [89] F. Provost and T. Fawcett, "Robust Classification for Imprecise Environments," *Mach Learn*, vol. 42, pp. 203–231, 2001, doi: https://doi.org/10.1023/A:1007601015854.
- [90] T. Fawcett, "An introduction to ROC analysis," *Pattern Recognit Lett*, vol. 27, no. 8, pp. 861–874, Jun. 2006, doi: 10.1016/j.patrec.2005.10.010.
- [91] V. Nykänen, I. Lahti, T. Niiranen, and K. Korhonen, "Receiver operating characteristics (ROC) as validation tool for prospectivity models - A magmatic Ni-Cu case study from the Central Lapland Greenstone Belt, Northern Finland," *Ore Geol Rev*, vol. 71, pp. 853–860, 2015, doi: 10.1016/j.oregeorev.2014.09.007.
- [92] V. Nykänen, I. Lahti, T. Niiranen, and K. Korhonen, "Receiver operating characteristics (ROC) as validation tool for prospectivity models - A magmatic Ni-Cu case study from the Central Lapland Greenstone Belt, Northern Finland," *Ore Geol Rev*, vol. 71, pp. 853–860, 2015, doi: 10.1016/j.oregeorev.2014.09.007. E. J. M. Carranza and A. G. Laborte, "Data-driven predictive mapping of gold prospectivity, Baguio district, Philippines: Application of Random Forests algorithm," *Ore Geol. Rev.*, vol. 71, pp. 777–787, 2015.